# 付録A.1　主な成果発表論文集

Sasano,Y., K. Asai, N. Sugimoto, Y. Kawamura, K. Tatsumi, and T. Imai, "NASDA Mission Demonstration Satellite lidar project and its sciences," Proc. SPIE, 3504, 2-7 (1998).

Liu, Z., P. Voelger and N.Sugimoto, "Simulations of the Observation of Clouds and Aerosols with the Experimental Lidar in Space Equipment (ELISE)," accepted for publication in Applied Optics (2000).

Voelger, P., Z. Liu, and N. Sugimoto, 1999: Effects of Multiple Scattering on the Retrieval of Optical Parameters from ELISE - Simulation Study, SPIE 3865, 172-177.

Invited Paper

# NASDA Mission Demonstration Satellite Lidar Project and its Sciences

Yasuhiro Sasano[a], Kazuhiro Asai[b], Nobuo Sugimoto[a], Yasuaki Kawamura[c], Kenji Tatsumi[c], and Tadashi Imai[c]

[a]National Institute for Environmental Studies, Tsukuba, Ibaraki 305-0053 Japan
[b]Tohoku Institute of Technology, Sendai, Miyagi 982-8577 Japan
[c]Research and Development Division, National Space Development Agency of Japan, Tsukuba, Ibaraki 305-8505 Japan

## ABSTRACT

In the Mission Demonstration Satellite Lidar (MDS-lidar) Project, the National Space Development Agency of Japan (NASDA) has started development of a satellite-borne lidar system for experiments in space, which is called Experimental Lidar-In-Space Equipment (ELISE). Its main purposes are to demonstrate technical feasibility of a space-borne lidar and its key components, and also to get scientific data on clouds/ aerosols distribution for better understanding of the earth climate system. Presentation will be made on the ELISE development plan, scientific goals and their implementation plan.

## 1. INTRODUCTION

The National Space Development Agency of Japan (NASDA) is planning to launch Mission Demonstration Satellites (MDS) in a series for verification of frontier missions and mission instruments in space, in order to meet demands for future missions which will be highly advanced and increasingly diversified, aiming at a quicker and cheaper way to test new technologies. As one of the MDS experiments, NASDA has decided to develop a lidar instrument for MDS-2 satellite (MDS-lidar project) in order to demonstrate its technical feasibility as well as possibilities of data use in atmospheric sciences, especially in climate change modelling studies. MDS-2 will be a small, single mission satellite. The lidar to be developed has been named as Experimental Lidar In Space Equipment (ELISE, for short).

ELISE is a Mie back scattering lidar to measure three-dimensional distribution of clouds and aerosols. ELISE aims at demonstrating technical feasibility, collecting data necessary for full-scale satellite-borne lidar systems in the future, and obtaining scientific data on clouds and aerosol distribution on a global scale. ELISE will employ an Nd:YLF that is pumped by diode lasers to generate 1053 nm and 527 nm lasers, analog and photon counting detection systems to enable daytime and nighttime continuous measurements, and a 1 m diameter receiving telescope.

Scientists at national government institutes and universities have gathered to establish a researcher's group to support the NASDA's project for MDS-lidar. The tasks of the group are to define science missions, develop data processing algorithms, plan validation experiments, conduct research on data analysis and utilization, and so on. The present report overviews the project and describes the research plans.

## 2. ELISE SPECIFICATION

Major specification of the MDS-lidar (ELISE) has been tentatively defined on the basis of scientific requirements and technical feasibility investigations. The laser to be employed is an LD-pumped Nd:YLF laser with its wavelengths of 1053 and 527 nm. The fundamental wavelength (1053 nm) will be used for detecting clouds as well as aerosols. The second harmonics (527 nm) will be used for getting aerosol information and air molecule signals for signal calibration. Its repetition rate is 100 pulse/sec and output energy per pulse is 84 mJ and 10 mJ for 1053 nm and 527 nm, respectively,

SPIE Vol. 3504 • 0277-786X/98/$10.00

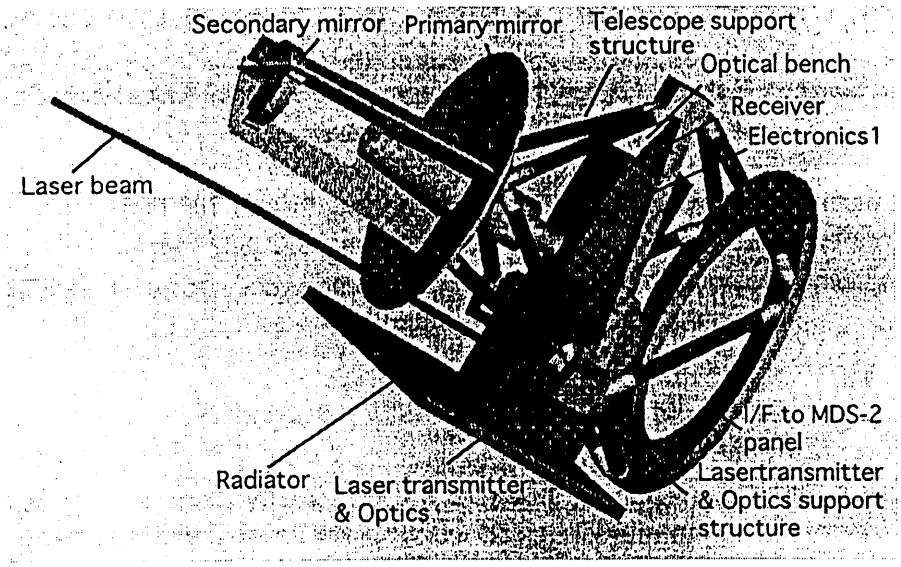


Figure 1 MDS-lidar (ELISE) layout without a light baffle

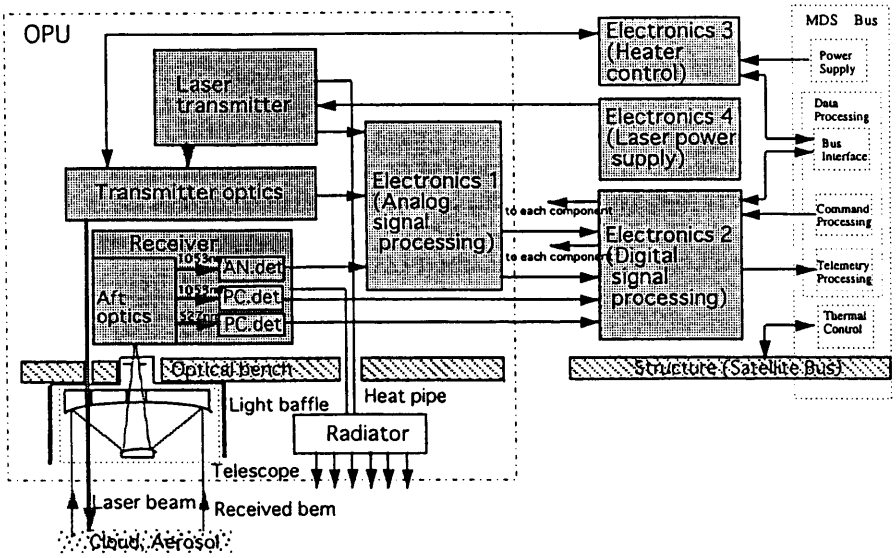


Figure 2 ELISE system diagram

which have been adopted on the basis of eye-safe consideration. The diameter of receiving telescope is 1 m. Figure 1 shows a conceptual layout of the ELISE and Figure 2 depicts a system diagram of ELISE. A tentative specification and expected performance of the ELISE system are shown in Table 1.

Two photon counting detection systems are used for 1053 and 527 nm signals, and one analog-mode detection system for 1053 nm signals. The analog-mode detection will be used mainly for continuous measurements of clouds in daytime and nighttime. A schematic diagram of the detection subsystem is shown in Figure 3.

Theoretical performance (S/N: signal to noise ratio) was calculated assuming an atmospheric model with a cirrus cloud layer (9 - 11 km) and a background aerosol layer (Table 2). A ground surface and a low-level cloud are assumed as a lower boundary which gives background signals. The actual S/N should depend not only on the instrument performance but also on the real atmospheric (cloud) and background conditions.

Table 2 indicates that an unrealistically huge amount of pulse integrations (more than a million pulses) is required for 1053 nm photon counting detection of air molecules at 35 km to get an S/N over 15. This is not meant to implement, but the 1053 nm photon counting detection will be used for aerosol detection, which may give information on wavelength dependence when combining 527 nm measurements.

The followings are considered as important issues that need further investigations and demonstration in space from engineering points of view:

a) thermal design of the laser oscillator which enables locally-generated heat to escape effectively, and thermal design of the satellite system

b) mirror design with little distortion under space conditions, manufacturing technology for ultra-lightweight mirrors, and technology for the polishing and testing of mirrors
c) enlargement of the dynamic range of the photon counting system, and a module design for mounting

Table 1. ELISE basic specification & performance(tentative)

| Item | | Specification (tentative) | Performance(Design] |
|---|---|---|---|
| Satellite | Orbit/height | Circular/about 550 km | 550±5 km |
| | Inclination angle | About about 30 deg. | 30 deg. |
| | Period | About about 95.7 min. | 95.645 min |
| | Ground speed | - | 6.983 km/s |
| Performance | Laser | LD pumped Nd:YLF laser | LD pumped Nd:YLF laser |
| | Wavelength | 1053.2 nm, 526.6 nm | 1053.2 nm, 526.6 nm |
| | Detection | Photon Counting (PC), Analog (AN) | PC, AN |
| | Vertical res. | 100 m (nominal) | 100 m (nominal) |
| | Horizontal res. | 1.5 km (AN,1053 nm) | 0.4 km (Integration 5)<br>1.45 km (Integration 20) |
| | | 150 km (PC,1053&527 nm) | 1.45 km (Integration 20)<br>14.1 km (Integration 200) |
| | Meas. range | 0 - 35 km | Dist. from ELISE : 510 - 560 km<br>< 0 km, > 35 km BG level |
| Transmitter | Wavelength | 1053.2 nm, 526.6 nm | 1053.2 nm, 526.6 nm |
| | Output Energy | 90 mJ (TBD), 4.4 mJ (TBD) | 8 4 mJ, 10 mJ (nominal) |
| | Pulse width | 40±10 ns | 67 ns (maximum) |
| | Pulse Rep. Rat | 100 pps | 100 pps (nominal) |
| | Beam divergence | 0.17 mrad | 0.17 mrad (nominal) |
| | Beam quality | Low order Gauss | Low order Gauss |
| | Stability (Short range) | ±3% / min | <±3% / min |
| Receiver | Eff. Diameter | 1,000 mm | nom. 1,000 mm |
| | IFOV | 0.21 mrad | nom. 0.22 mrad |
| | Filter band width | 0.3 nm (AN), 10 nm (PC) | max 0.3 nm (AN]<br>max 4 nm (PC) |
| | Transmission | - | 40 % (AN)<br>6.5 % (PC, 1053 nm)<br>60 % (PC, 527 nm) |
| | Quantum efficiency | 36 % (AN) | 31.5 % (AN) |
| | Det. probability | 1.5 % (PC, 1053 nm)<br>39 % (PC, 527 nm) | 1.25 % (PC, 1053 nm)<br>34 % (PC, 527 nm) |
| | Dynamic range | AN: > 25 dB, PC: > 1 Mcps | 25 dB (AN) (minimum)<br>4 Mcps (PC) (minimum) |
| | Data bits length | - | 12 bits / Data |
| Mass <250 kg | | < 250 kg | 250 kg |
| Volume | | - | 1,600 x 1,430 x 2,600 mm |
| Power required | | < 250 W | 295 W |

Table 2. Expected performance (nominal S/N ratio)

| Detection | | Wavelength | Target | Day/Night | Lower boundary | S/N (Integration) |
|---|---|---|---|---|---|---|
| (1) | AN | 1053 nm | Cirrus | | | |
| | | | ( $\beta$ = 3.0 E-5 $m^{-1}$ at its peak, h = 9 - 11 km) | | | |
| | | | | Day | Low Cloud | 14.2 (Int.20) |
| | | | | Day | Ground Surface | 22.5 (Int.20) |
| | | | | Night | Low Cloud | 32.0 (Int.20) |
| (2) | PC | 527 nm | Air molecules at 35 km | | | |
| | | | | Night | Low Cloud | 4.1 (Int.2000) |
| | | | | Night | Ground Surface | 19.0 (Int.2000) |
| (3) | PC | 1053 nm | Air molecules at 35 km | | | |
| | | | | Night | Low Cloud | 17.4 (Int.1.6E6) |

Day: daytime measurements,
Night: nighttime measurements
nom.: nominal condition value
Int: integration number of pulses

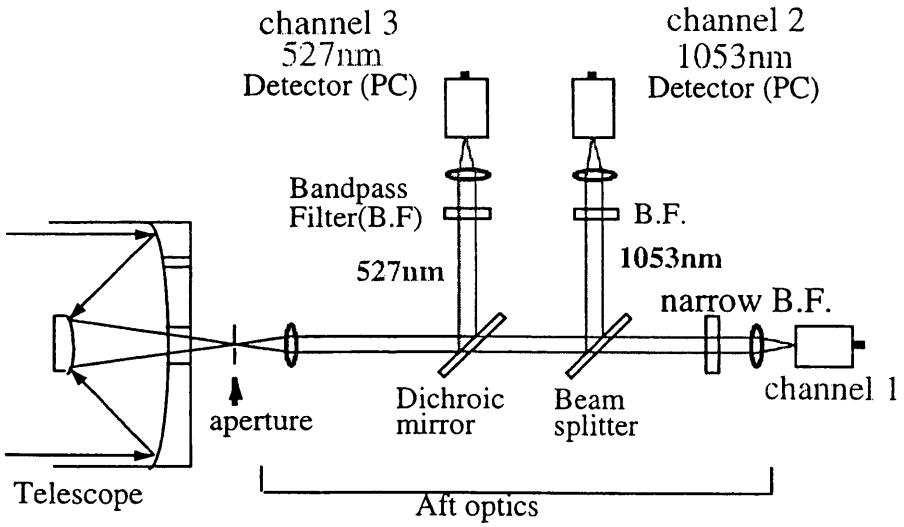


Figure 3 MDS-lidar (ELISE) receiver schematics

NASDA is developing bread-board models of some of the key components such as a laser, a photon counting system and so on. The ELISE TFM (Test and Flight Model) will be manufactured to be ready for installation on board a satellite in early 2000's. Drawings for ELISE are shown in Figure 4.

## 3. SCIENTIFIC MISSION

One of the main difficulties in accurately predicting future global warming is considered to be caused by the lack of scientific knowledge on the distribution of clouds and their interaction with climate. Low-altitude clouds scatter solar radiation (umbrella effect) and lower the temperature in the lower atmosphere. On the other hand, cirrus and other high-altitude thin clouds not only have an umbrella effect, but also absorb long-wave radiation from the ground surface and the lower atmosphere, thus producing a greenhouse effect as well. The actual effect of clouds depends on the size of cloud droplets, height frequency of cloud appearance, optical depth, and so on, which are not yet well understood.

Model inter-comparison studies on future climate prediction have shown that models with different treatment of clouds produce large discrepancies and uncertainties in the predicted temperature rise. To solve this problem, it is important to correctly understand the actual situation of cloud appearance and clarify the relationship between cloud distribution and

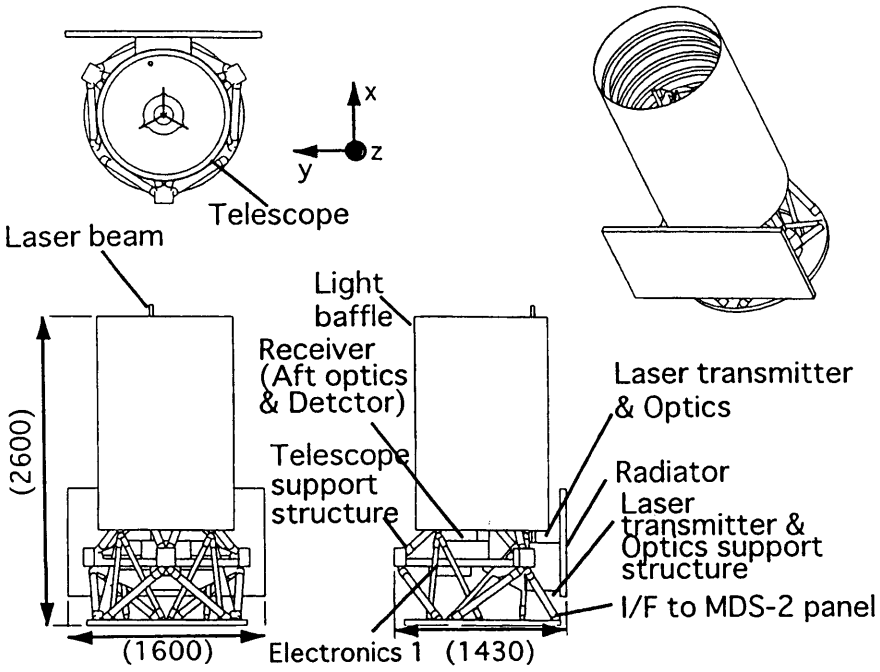


Figure 4 Drawings for ELISE

radiative balance. Multi-layered structures of cloud distribution and distribution of high-altitude (cirrus) clouds must especially be investigated. Interaction between aerosols and clouds is another important factor to understand the formation process and optical properties of clouds. Thus the aerosol distribution must be investigated on a global scale, paying particular attention to its interaction with clouds.

Space-borne lidars have been investigated as an effective measurement tool for these purposes. In 1994, a research group at the NASA Langley Research Center successfully conducted an experiment (LITE) of lidar measurements from the Space Shuttle, which demonstrated vividly the effectiveness of space-borne lidars. As the LITE experiments have shown, lidar measurements from space provide a lot of valuable information on atmospheric phenomena through clouds/aerosol three-dimensional distribution data.

Major scientific objectives of ELISE experiments are to obtain detailed information on high altitude thin clouds (cirrus), multi-layered clouds structures, and aerosol distributions over the globe. Since the MDS-2 will be a single mission satellite, information on cloud optical characteristics will be derived from combination of data obtained with other satellites and ground-based measurements. These analyses will be made in parallel with validation experiments and analyses. Validation experiments will be conducted by employing mainly ground-based lidars and airborne lidars.

The following fields of studies would be very interesting and productive:

- identification and climatological (statistical) analysis of the vertical distribution and multi-layer structure of clouds
- climatological (statistical) analysis of upper clouds and cirrus clouds
- identification of clouds and the radiation balance by conducting simultaneous ground-based observations
- research on the formation process of cirrus clouds, such as validation of a formation process model, by understanding the structure of cirrus clouds
- wide-area three-dimensional distribution of tropospheric aerosols
- wide-area distribution of stratospheric aerosols and the atmospheric circulation

Requirements to data acquisition and processing are under study by the researchers group. The basic idea regarding on-board data acquisition is shown in Table 3 (in the previous page), which was prepared by NASDA. Full utilization of a recording device will be requisite since opportunities of downlink to a ground station are quite limited. Therefore it is quite important to establish a strategic data acquisition plan to compromise requests to get a climatological data set with global coverage and to get detailed information on cloud/aerosol spatial distribution.

Table 3. Data acquisition plan (tentative)

| | | | | |
|---|---|---|---|---|
| Memory capacity of data recorder | | | 1 Gbits assumed | |
| Total data acquired per day | | | | |
| Bit rates of down link | | | 1 Mbps | |
| Visible time per day | | | about 18 min. (= 6 min x 3 times) | |
| Total data | | | about 1 Gbits (=1 Mbps x 18 min x 60 sec) | |
| Data mode (Example) | | | | |
| Mode | Integration AN | Integration PC | Data rate | Observation time (Memory capacity of 1 Gbits) |
| Obs. Mode I | 5 | - | 134.24 kbps | 124 min |
| (AN 1 ch.) | 20 | - | 33.56 kbps | 497 min |
| Obs. Mode II | - | 20 | 63.56 kbps | 267 min |
| (PC 2 ch.) | - | 200 | 6.36 kbps | 2622 min |
| Obs. Mode III | 5 | 20 | 194.24 kbps | 86 min |
| (AN 1 ch. +PC 2 ch.) | 5 | 200 | 140.24 kbps | 119 min |
| | 20 | 20 | 93.56 kbps | 178 min |
| | 20 | 200 | 39.56 kbps | 420 min |
| Alignment Mode | - | 20 | 33.56 kbps | 497 min |
| Vertical resolution:100 m | | | | |
| Horizontal resolution dependent on integration times: 1.45 km for integration of 20 pulses | | | | |

## 4. ACKNOWLEDGEMENT

The author express his sincere thanks to the members of Mission Demonstration Satellite Lidar Team of ESTO/Forum for their active discussion in the preparation phase of the project and to the staff at the NASDA R&D Division for their efforts in the engineering aspects of the project.

## 5. REFERENCES

1. Y. Sasano and T. Kobayashi (ed.) : Feasibility study on space lidars for measuring global atmospheric environment No. 4 Final Report, F-82-'95/NIES, 1995 [available from NIES]

2. MDS Lidar Team (ed.) : Proceedings of the first workshop on Mission Demonstration Satellite Lidar, (Hakone, Japan, March 11, 1998), 97MOA2-D001, 1998 [available from ESTO]

Accepted for publication in *Applied Optics* (2000)

# Simulations of the Observation of Clouds and Aerosols with the Experimental Lidar in Space Equipment (ELISE)

Zhaoyan Liu, Peter Voelger and Nobuo Sugimoto

National Institute for Environmental Studies, 16-2 Onogawa, Tsukuba,
Ibaraki 305-0053, Japan

**Abstract**

We carried out a simulation study for the observation of clouds and aerosols with the Japanese Experimental Lidar in Space Equipment (ELISE) which is a two-wavelength backscatter lidar with three detection channels. It was planned by the National Space Development Agency of Japan for launch on the Mission Demonstrate Satellite 2 (MDS-2). In the simulations, the lidar return signals for ELISE are calculated for an artificial, two-dimensional atmospheric model including different types of clouds and aerosols. The signal detection processes are simulated realistically by including various sources of noise. The generated lidar signals are then used as input for simulations of data analysis with developed inversion algorithms to investigate the retrievals of optical properties of clouds and aerosols. The results demonstrate that ELISE can provide global data on structures and optical properties of clouds and aerosols. We also conducted an analysis of the effects of cloud inhomogeneity on retrievals from averaged lidar profiles. It is shown that the effects are significant for space lidar observations of optically thick broken clouds.

Key words: Lidar, Space lidar, Backscattering, Cloud and aerosol measurements

## 1. Introduction

Clouds and aerosols significantly influence the earth's climate through scattering and absorption of radiation. The radiative effect of clouds strongly depends on their vertical distributions. Aerosols affect radiative processes not only directly through scattering and absorption of radiation but also indirectly through formation of clouds by altering the number of cloud condensation nucleus and the size of cloud particles. However, our knowledge of the distribution of aerosols, the process of cloud formation, the vertical structure of clouds, and the radiative feedback of clouds and aerosols is rather incomplete. Consequently, in climate models these processes are only dealt with in an approximate manner, which causes uncertainties in the model predictions.[1] Space-borne lidar is a very effective tool for observing the global distribution of clouds and aerosols as demonstrated by the Lidar In-space Technology Experiment (LITE)[2] and therefore is useful for the validation of climate models and for process studies related to climate change.

In recent years the National Space Development Agency of Japan (NASDA) has been developing the so-called Experimental Lidar in Space Equipment (ELISE)[3,4] for launch on the Mission Demonstration Satellite-2 (MDS-2). The ELISE program has a two-fold objective. The first target is to demonstrate the technical applicability of the key components of the lidar system in space. The second target is to apply the collected data to scientific studies. The observations are aimed at high-altitude clouds (cirrus), multiply-layered cloud systems and stratospheric and tropospheric aerosols. As a part of the prelaunch studies for ELISE, we studied signal inversion algorithms for space-borne lidars and conducted simulations for measurements with ELISE. In this paper we describe the simulation study for the observation of clouds and aerosols with ELISE. In our study we simulated lidar return signals for an artificial two-dimensional model containing clouds and aerosols. The obtained signals are used as input for inversion simulations in order to investigate retrievals of cloud and aerosol optical properties utilizing developed algorithms.

In the following section we describe the system characteristics of ELISE. In Section 3, simulations of lidar return signals are presented. Optical properties of different kinds of clouds and aerosols are reviewed, and the two-dimensional cloud and aerosol distribution model is constructed. Detection of lidar return signals with ELISE is then simulated including all possible noise sources. Section 4 describes the method for calibrating ELISE system. In Section 5, we discuss the methods for cloud detection with ELISE data. Section 6 deals with the retrievals of optical properties of clouds and aerosols. We analyze the effects of cloud inhomogeneity on retrievals of cloud optical properties and cloud vertical distributions from averaged lidar profiles, which is significant for space lidar observations of optically thick broken clouds, in Section 7.

## 2. Outline of ELISE

ELISE is a nadir-looking two-wavelength, three-channel backscatter lidar that will provide along-track cloud and aerosol observations. Major specifications of ELISE have been defined by NASDA as listed in Table

1.[3,4] The planned orbit for ELISE is sun-synchronous with an inclination angle of 97.59', i.e., it covers most part of the globe. The transmitter of ELISE uses a laser diode (LD) pumped Nd:YLF laser as a light source with the fundamental output at 1053.2 nm and the second harmonic at 526.6 nm. The receiver has three detection channels. One is an analog detection (AN) channel to detect the backscattered laser light at 1053 nm. The other two are photon counting (PC) channels at 1053 nm and 527 nm, respectively. The AN channel will be operating during both daytime and nighttime, and PC channels will be operating only in the night. All detection channels use space qualified silicon avalanche photodiodes (Si-APDs) which were designed by EG&G CANADA LTD., Toronto.

Output energy of the transmitted laser is 84 mJ at 1053 nm and 10 mJ at 527nm. Pulse repetition rate is 100 Hz. Lidar signals are accumulated for 20 or 60 laser shots for the AN channel (that corresponds to 1.4 km or 4.2 km horizontal resolution), and 20 or 300 shots for the PC channels (1.4 km or 21 km). The detection mode with shorter averages is the preferred option. However, due to the limited data transmission rate between satellite and ground station longer averaging has to be applied for a certain amount of time. The vertical resolution of the measurements is 100 m. The system parameters in Table 1 are used in the simulation study described in the following sections.

Table 1 ELISE major specifications (design)

| | |
|---|---|
| Satellite | |
| Orbit: | sun-synchronous circular |
| height: | 550±5 km |
| Ground speed: | 6.983 km/s |
| Period: | 95.6 minutes |
| Inclination angle: | 97.59 degree |
| Transmitter | |
| Laser: | LD-pumped Nd:YLF (fundamental and second-harmonic) |
| Output energy: | 84 mJ at 1053 nm; 10 mJ at 527 nm |
| Pulse repetition rate: | 100 Hz |
| Beam divergence: | 0.17 mrad (full angle) |
| Receiver | |
| Effective diameter: | 1000 mm |
| Field of view (FOV): | 0.21 mrad (full angle) |
| Filter bandwidth: | AN: 0.3 nm; PC: 4 nm |
| Transmission: | 47% (AN, 1053 nm); 7% (PC, 1053 nm); 67% (PC, 527 nm) |
| Detector: | Si-APD * |
| Quantum efficiency: | 45 % (AN, 1053 nm) |
| Detection probability: | 1.25 % (PC, 1053 nm); 34 % (PC, 527 nm) |
| Dynamic range: | AN: 8 bits; PC: 4 Mcps |
| Measurement | |
| Direction: | nadir |
| Height coverage: | earth surface ~ 35 km |
| Vertical resolution: | 100 m |
| Horizontal resolution: | AN: 1.4 km/4.2 km; PC: 1.4 km/21 km |

* The Si-APD is made by EG&G for space operation. The dark count at maximum is 500 $s^{-1}$ for photo-counting; the dark current is $1.31 \times 10^{-12}$ A $Hz^{-1/2}$ for analog; the excess noise factor is 4; and the multiplication factor is 100.

## 3. Simulation of Lidar Signals Measured with ELISE

In this section we first describe the model atmosphere for the simulation, followed by a discussion of the simulation of the lidar signals for ELISE.

### A. Model Atmosphere

Clouds and aerosols are the main targets of observations with ELISE. Because ELISE has a global coverage, various cloud and aerosol types must be considered in our simulations. Table 2 summarizes typical scattering parameters of different clouds and aerosols, namely, the volume backscatter coefficient $\beta$, the lidar ratio $S$ (i.e., the extinction-to-backscatter ratio), the wavelength dependence parameter for aerosol backscattering $\alpha$ which is defined by $\beta(\lambda_1)/\beta(\lambda_2)=(\lambda_1/\lambda_2)^{-\alpha}$, and the depolarization $\delta$ (although not observed with ELISE).

The lidar ratio is a key parameter for the lidar signal inversion. For cirrus clouds, $S$ has been found to vary over a range from less than 10 to larger than 100 sr due to large variations in particle shape.[5-8] Numerical calculations by Takano and Liou[9,10] showed that the lidar ratio is ~10 sr for solid hexagonal and 20-100 sr for hollow ice crystals. Cirrus clouds usually are optically thin with a typical optical depth of 0.1-0.2.[7] In addition,

observations[2,7] and theoretical predictions[9] showed that for cirrus cloud with large ice crystals, the scattering parameters are usually not or only very weakly wavelength-dependent in the visible and near-infrared regions. However, for high altitude thin cirrus in the Antarctica region, a strong wavelength-dependence has been observed.[8] This exception is a result of the mixture of ice crystals with sulfuric haze particles with small size at submicron or micron.

The lidar ratio of water clouds is less variable than that of cirrus. It shows only little droplet size dependence in the visible and near-infrared regions.[11,12] Pinnick et al.[11] presented a theoretically calculated value of 18.2 sr at 1.06 μm and a measured value of 17.7 sr at 0.6328 μm for laboratory-generated clouds. We therefore concluded that a similar value can be applied in our investigation.

Table 2 Typical scattering parameters of clouds and aerosols in visible and near infrared regions

| Type | Backscatter [a] $\beta$ [$m^{-1}sr^{-1}$] | Lidar ratio $S$ [sr] | Wavelength dependence parameter, $\alpha$ | Depolarization $\delta$ |
|---|---|---|---|---|
| Cirrus | $1x10^{-6}$ - $2.5x10^{-4}$ | 5 - 100 | ~ 0 | 0.1 - 1.0 |
| Water clouds | $5x10^{-5}$ - $5x10^{-3}$ | 15 - 20 | ~ 0 | 0 |
| PSC, type $I_a$ | $1x10^{-8}$ - $4x10^{-8}$ | ? | 0.4 | 0.3 - 0.5 |
| PSC, type $I_b$ | $1.5x10^{-7}$ - $8x10^{-7}$ | | 2 - 3 | 0.005 - 0.04 |
| PSC, type II | > $2.5x10^{-7}$ | | < 0.8 | > 0.1 |
| Stratospheric aerosols | $1x10^{-9}$ - $6x10^{-7}$ | 20 - 70 | 1.0 - 2.0 | ~ 0 |
| Kosa (yellow sand) | $2x10^{-6}$ - $2x10^{-5}$ | 30 - 100 | ? | 0.1 - 0.2 |
| Tropospheric aerosols | $2x10^{-6}$ - $2x10^{-5}$ | 20 - 80 | 0.65 - 1.25 | < 0.05 |

[a] Backscatter coefficient at 527 nm.

There are two types of polar stratospheric clouds (PSCs). They can be distinguished by lidar from the magnitude of the backscatter[13] and depolarization, though depolarization will not be measured with ELISE. For Type I clouds it is generally assumed that they are composed of nitric acid trihydrate (NAT); Type II clouds are water ice clouds. Type II particles are not spherical in shape and have larger backscatter than that of Type I. Two subtypes of Type I PSCs, $I_a$ and $I_b$, were observed.[14] Type $I_a$ has large depolarization and low backscatter ratio (aerosol and molecular backscatter to molecular backscatter) with low wavelength-dependence, indicating that Type $I_a$ particles are not spherical. Type $I_b$ particles are spherical or nearly spherical.

The stratospheric aerosol consists of sulfuric acid droplets. In fresh volcanic aerosol plumes the total number of particles is increased and the particle size has to be characterized with a bimodel distribution due to the significant injection of large size particles. Calculations based on in situ stratospheric aerosol measurements

showed variable lidar ratios depending on both time and height; the range of reported lidar ratio is 22-63 sr at 532 nm and 26-67 sr at 1064 nm for the 1980-1987 period.[15] A model study[16] based on lidar observations predicted that lidar ratio at 532 nm is 52 sr for the background and 40 sr for the volcanic stratospheric aerosols, respectively.

In the troposphere aerosol mixtures strongly depend on regional sources. Due to different compositions the lidar ratio can vary over a wide range.[17,18] Additionally, relative humidity alters scattering properties of aerosols. To show the influence of relative humidity Fig.1 presents theoretically calculated lidar ratio $S$ and wavelength dependence parameter $\alpha$ at both wavelengths of ELISE for aerosol types as given in the OPAC data set.[19]

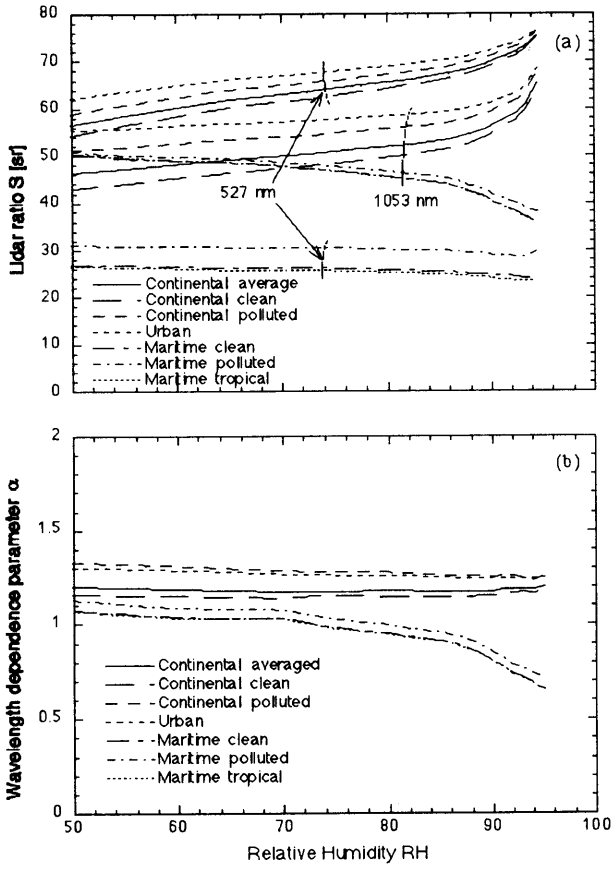


Figure 1 Theoretically calculated lidar ratios S (a) and wavelength dependence parameter of the backscatter coefficient α (b) of different aerosol types as a function of relative humidity.

As shown in Fig.1, lidar ratios vary in the range between 23 and 76 sr at 527 nm and between 35 and 68 sr at 1053 nm, while wavelength dependent parameters are within ranges of 1.15-1.25 for urban and continental type and 0.65-1.13 for maritime type aerosols. Aerosols which mostly consist of nonhygroscopic particles (e.g., minerals) are not considered in Fig.1, since their optical properties show almost no dependence on the relative humidity. Kosa (Asian dust or 'yellow sand') is an example for such a layer. It consists of large, nonspherical particles.[20] This results in large lidar ratio (up to 100 sr) and large depolarization (0.1-0.2).

We developed a two-dimensional atmospheric model in order to simulate ELISE return signals and to test lidar signal inversion methods. Figure 2(a) shows the modeled backscatter distribution at 527 nm. It includes stratospheric aerosols, tropospheric aerosols (Planetary Boundary Layer (PBL) below 1.2 km and a Kosa layer between 3 and 5 km altitudes), a cirrus cloud between 10 and 12 km altitudes and several low-altitude water clouds with different structures. The model also includes molecules based on the U.S. Standard Atmosphere. To simplify the calculation, we assumed that the wavelength dependence of backscatter is $\lambda^0$ for clouds and $\lambda^{-1}$ for aerosols. This assumption does not have a large impact on the simulation of lidar signals and the testing of lidar inversion algorithms. To examine the effect of lidar ratio on the retrievals, we assumed spatially changing lidar ratios as shown in Fig. 2(b). We used sinusoidal variations with an amplitude of 25% of the median value. The median value is 20 sr for clouds and 50 sr for aerosols.

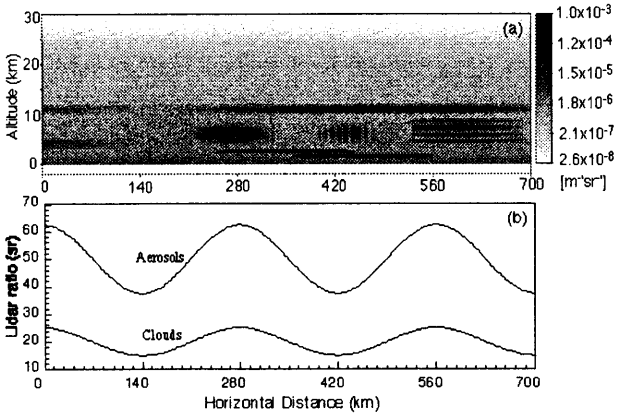


Figure 2 An artificial atmospheric model: (a) backscatter distribution at 527 nm; (b) lidar ratios. A wavelength dependence of $\lambda^0$ for clouds and $\lambda^{-1}$ for aerosols is assumed. A stratospheric aerosol layer is centered at 20 km altitude; a Kosa layer is between 3 and 5 km altitudes and 0 and 140 km horizontal distances; a PBL is below 1.2 km altitude; a cirrus layer is between 10 and 12 km altitudes; and several low and mid-altitude water clouds are distributed below the cirrus.

B. Generation of Lidar Signals

The received lidar signal due to the aerosol and molecular scattering is described by the lidar equation

$$N_s(r) = \frac{1}{r^2} C \cdot \left[\beta_1(r) + \beta_2(r)\right] \cdot T^2(r) \quad , \tag{1}$$

where subscripts 1 and 2 refer to the aerosol and molecular scattering, respectively. $N(r)$ is the received signal photoelectron number from range $r$ , $\beta(r)$ is the volume backscatter coefficient at $r$. $T(r)$ is the atmospheric optical transmission along the path from lidar to $r$. It can be written as

$$\exp\left(-\int_{r_0}^{r}\left[\sigma_1(r) + \sigma_2(r)\right]dr'\right),$$

if multiple scattering is not considered. $\sigma(r)$ is the extinction coefficient $r$. $C$ is the lidar constant which contains lidar system parameters and other range-independent quantities. It can be written as

$$C = E_0 A_0 k\eta \frac{c\Delta t}{2} \frac{\lambda}{hc} . \tag{2}$$

Here, $E_0$ is the laser output energy per pulse, $A_0$ the receiving telescope area, $k$ the total optical efficiency of the lidar transmitter and receiver, $\lambda$ the laser wavelength, $c$ the light speed, and $h$ the Planck's constant. $\eta$ is the quantum efficiency of the detector for AN or the detection probability for PC with an APD. $\Delta t$ is the sampling time.

Detected lidar return signals include not only the backscattered signal as given by Eq. (1) but also the background radiation and the detector noise. For PC mode, the standard deviation of detected photon count for single laser shot can be written as

$$\delta N(r) = \left[N_s(r) + N_b + N_d\right]^{1/2} . \tag{3}$$

Here $N_S$ is the photon count number of the received scattering signal which can be calculated from Eq.(1). $N_d$ is the dark count of the detector within sampling time $\Delta t$. It can be determined from the dark count rate $N_{d0}$ of the detector, $N_d = \Delta t N_{d0}$. $N_{d0}$ is a parameter of the detector generally provided by the manufacturer. $N_b$ is the received number of photon counts due to diffuse radiation. It is given by

$$N_b = I_b A_0 \Delta\lambda \Delta t k\eta \frac{\phi^2\pi}{4} \frac{\lambda}{hc} , \tag{4}$$

Here, $I_b$ is the solar spectral radiance reflected from the atmosphere and earth's surface, $\Delta\lambda$ is the bandwidth of the interference filter of the receiver, $\phi$ is the receiver field-of-view (FOV). For AN mode with a Si-APD, the standard deviation of the detected photoelectron number is given by 21

$$\delta N(r) = \left[\left(N_s(r) + N_b\right)F_m + \frac{I_{APD}^2 \Delta t}{M^2 q^2}\right]^{1/2} , \tag{5}$$

where $F_m$ , $I_{APD}$ and $M$ are the excess noise factor, the noise current and the multiplication factor of Si-APD, respectively. These parameters are generally also provided by the manufacturer. $q$ is the electron charge.

Different methods are used for AN and PC channels to generate lidar signals including noise. For AN detection, the following equation holds:

$$N(r) = N_s(r) + \delta N \cdot N_{ran} . \tag{6}$$

Here $N_{ran}$ is a normally distributed random number having a mean of zero and a standard deviation of 1. The lidar signal consequently has a mean value of $N_S(r)$ and a standard deviation of $\delta N(r)$. Lidar signals for all range bins are calculated with Eqs. (1), (2) and (4)-(6), and then digitized. Both the digitization noise and the effect of possible overflow are included in the simulation process.

In the PC mode where the number of received photoelectrons is generally small, individual photoelectron signals are discriminated and counted. The theoretically calculated photoelectron number, $[N_S(r)+N_b+N_d]$, which sometimes is smaller than one, defines a probability. This means that the averaged received photoelectron number for a great number of the same measurements is $[N_S(r)+N_b+N_d]$, and the standard deviation is $[N_S(r)+N_b+N_d]^{1/2}$. However, the number of received photoelectrons for each measurement is a natural

number or zero. In order to simulate the single-shot received signal, the method described as follows is used. To get one signal for the measurement of each range bin, $n0$ times of the same measurements are considered. $n0$ is given for the range bin so that $n0[N_S(r)+N_b+N_d]$ is sufficiently large (e.g., several hundreds or larger). Then the $n0[N_S(r)+N_b+N_d]$ photoelectrons are distributed among the $n0$ measurements randomly. A random number generator that gives uniformly distributed pseudo-random numbers is used to distribute the photoelectrons. The received signal for a single shot is obtained by choosing one of the distributed photoelectron numbers. The signals simulated in this way have a mean photo-count number of $[N_S(r)+N_b+N_d]$ and a standard deviation of $[N_S(r)+N_b+N_d]^{1/2}$. Signals for other range bins are generated independently in the same way. Similarly, lidar profiles at different locations are calculated to obtain a two-dimensional set of simulation data. Saturation in the photon counting must be considered when the count rate of the return signal is larger than about $1\times10^6$ [$s^{-1}$]. Saturation is a main source of error for strong returns in measurement with PC channels. The effect of saturation is also included in the simulations of detection with PC channels.

We simulated lidar signals from the modeled atmosphere shown in Fig. 2 for the three channels of ELISE. The system parameters were used as given in Table 1. We assumed the moonlit cloud condition for nighttime and sunlit cloud condition for daytime;[22] the spectral radiances during night-time are $0.17\times10^{-6}$ and $0.46\times10^{-6}$ (W $m^{-2}sr^{-1}nm^{-1}$) for 1053 nm and 527 nm, respectively. During daytime they are $10^6$ times larger.

The simulated lidar signals are shown in Fig. 3. Each profile was integrated over 20 laser shots. In this simulation, multiple scattering was not considered. The effect of multiple scattering will be investigated in a more quantitative discussion in the future. The maximum and minimum of the gray scale for each panel are taken at the maximum and minimum detectable photo-electron numbers for both PC and AN channels. For PC channels, they are 160 and 1, respectively. In the analog detection, a 8-bit digitizer is used, and the sensitivity is adjusted so that the full scale is at the signal level as scattered from a target with a backscatter coefficient of 0.1 ($km^{-1}$ $sr^{-1}$).
In the case of the 527-nm PC channel data acquisition saturation is caused by clouds and the earth's surface. Saturations is also seen in the 1053-nm PC and AN signals from low altitude optically thick clouds and from the surface.

It can be seen from Fig.3 that cloud structures can be observed with all three channels except for the optically thin part of the cirrus cloud and the lower part of optically thick clouds where the laser beam cannot penetrate completely. Aerosol layers in the troposphere can be observed even if there are cirrus clouds above. Stratospheric aerosols can be detected only with the 527-nm PC channel.

For a more detailed discussion Fig. 4 shows examples of the lidar profiles for the atmospheric model at the horizontal location of 0 (Fig. 2). The modeled backscatter coefficients at the two wavelengths, the noise-free lidar signals (scattered signals and background light) for all three channels, and the SNRs are indicated. The cloud and aerosol signals are largest in the 1053-nm AN channel. However, the 527-nm PC channel has the highest SNR. The SNR of the 1053-nm PC channel is also larger than that of the 1053-nm AN channel except for the cirrus layer. The low SNR in the AN channel is due to the noise current in the Si-APD.

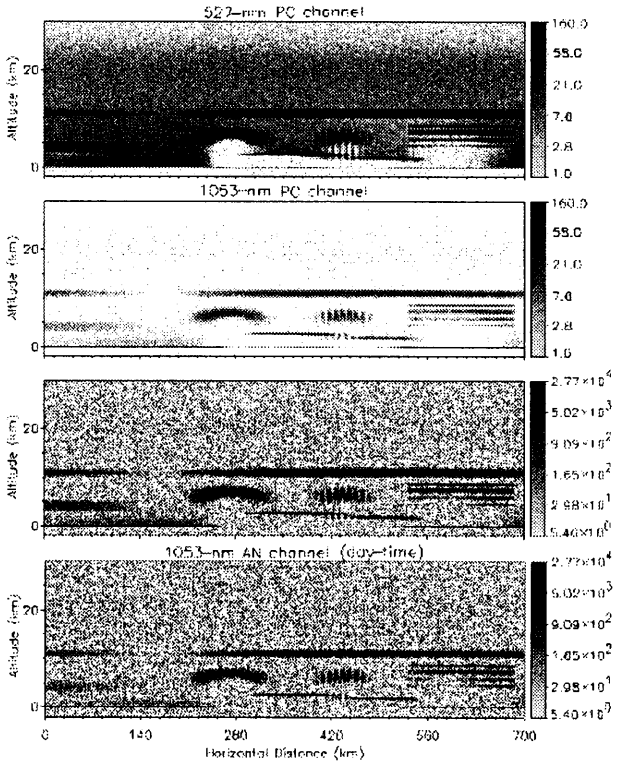


Figure 3 Simulated lidar return signals (photo-electron counts) from the model atmosphere shown in Fig.2. Each profile was integrated for 20 laser shots and the vertical resolution is 100 m.

To discuss the performance of each channel quantitatively, noise contributions of the background radiation, the dark count or dark current calculated with Eqs. (3)-(5) are summarized in Table 3. The signal noise (photon noise) is also listed in Table 3 for the Rayleigh scattering signal from an altitude of 35 km. For the 527-nm PC channel the signal noise and the background noise are dominant; for the 1053-nm PC channel the dark count noise is of the same magnitude as the signal and background noise. The dark current noise is dominant in the 1053-nm

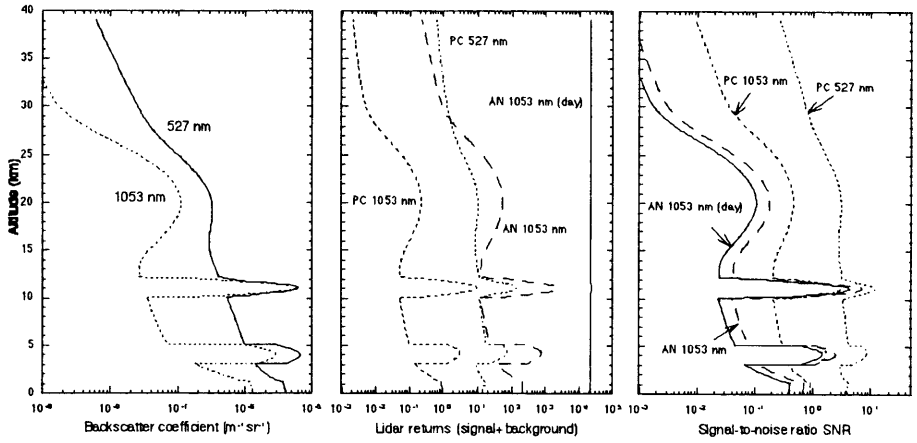


Figure 4 Modeled backscatter profiles at two wavelengths at the horizontal distance of 0 (a), lidar return profiles (scattering signal and background light) in units of photo-electron counts (b), and signal-to-noise ratios (c).

Table 3 Noise level in lidar signals (photoelectron number) caused by the background lights, the dark counts or noise currents and the scattering signal at 35 km.

| Channel | Background [a] $\mathcal{N}_b$ | Dark count [b] $\mathcal{N}_d$ | Noise current [c] $\mathcal{N}_d$ | Signal noise (35 km) $\mathcal{N}_s$ |
|---|---|---|---|---|
| PC 527 nm (night) | 0.149 | 0.0183 | - | 0.143 |
| PC 1053 nm (night) | 0.00791 | 0.0183 | - | 0.00908 |
| AN 1053 nm (night) | 0.135 | - | 66.9 | 0.565 |
| AN 1053 nm (day) | 135 | - | 66.9 | 0.565 |

a Spectal radiance: $0.17 \times 10^{-6}$, $0.46 \times 10^{-6}$ ($W\ m^{-2} sr^{-1} nm^{-1}$) for 1053 nm and 532 nm (night); 0.17 ($W\ m^{-2} sr^{-1} nm^{-1}$) for 1053 nm (day).

b Dark count rate of Si-APD for the PC detection mode: 500 ($s^{-1}$).

c Noise current of Si-APD for the AN detection mode: $1.31 \times 10^{-12}$ ($A\ Hz^{-1/2}$).

AN channel in the nighttime, but the background noise exceeds the dark current in the daytime, though they are comparable. The performance of this channel consequently is not very different in the daytime and nighttime.

## 4. Calibration of ELISE System

Before describing data reduction methods in the following sections, we discuss the method for calibrating ELISE system which is essential in some of data analysis methods. In the calibration, the lidar system constant, i.e., constant $C$ in Eq.(1), must be determined for each detection channel. For the 527-nm PC channel, the lidar constant can be determined with the Rayleigh scattering signal from a 30-35 km altitude range. Above 30 km the lidar return signal can be considered as only due to molecular scattering whose scattering parameters can be obtained from radio-sonde pressure and temperature data.

From the lidar equation, $C_{PC,527}$ can be determined by

$$C_{PC,527} = \frac{1}{n} \cdot \sum_{r_i=H-35km}^{H-30km} \frac{X(r_i)_{PC,527}}{\beta_{2,527}(r_i) \cdot T_{527}^2(r_i)}, \tag{7}$$

where $X(r)=N_S(r)r^2$, $H$ is the satellite height, and $n$ is the number of height intervals between 30 and 35 km altitude. $T(r)$ is the atmospheric transmission from the lidar to altitudes 30-35 km. It can be estimated from a standard atmospheric model or observation data as discussed in the following error analysis.

The 1053-nm PC channel can be calibrated relatively with the Rayleigh scattering signals in both PC channels from a 30-35 km altitude range. The ratio of lidar constants for 1053-nm and 527-nm PC channels can be written as

$$\frac{C_{PC,1053}}{C_{PC,527}} = \frac{\sum_{r_i=H-35km}^{H-30km} X(r_i)_{PC,1053} / T_{1053}^2(r_i)}{\sum_{r_i=H-35km}^{H-30km} X(r_i)_{PC,527} / T_{527}^2(r_i)} \cdot \left(\frac{1053}{527}\right)^4. \tag{8}$$

If the Rayleigh scattering signal is obtained with a sufficient SNR at 1053 nm, the lidar constant for 1053 nm PC channel can be determined with Eq. (8). Since Eq.(8) does not include the molecular backscatter coefficient, this ratio can be determined accurately by averaging lidar profiles over a large horizontal distance without considering the variation of the molecular density.

The sensitivity of the 1053-nm AN channel is too low to detect Rayleigh scattering signal from a 30-35 km altitude range. However, the ratio of the lidar constants for the 1053-nm AN and PC channels can be simply determined from the ratio of the two signals from cirrus clouds or aerosol layers with suitable backscatter coefficient as demonstrated in the following simulation with generated lidar signals. Although the signals from optically thick clouds or earth surface have high intensity, they are not suitable for calibration because they can be saturated.

The uncertainties of the determined lidar constants can be derived from Eqs. (7), (8):

$$\frac{\delta C_{PC,527}}{C_{PC,527}} = \frac{\left\{ \sum_{r_i=H-35km}^{H-30km} \left( \frac{X(r_i)_{PC,527}}{\beta_{2,527}(r_i) \cdot T_{527}^2(r_i)} \right)^2 \left( \frac{1}{n_0} \left( \frac{\delta X_{PC,527}(r_i)}{X_{PC,527}(r_i)} \right)^2 + \left( \frac{\delta \beta_{2,527}(r_i)}{\beta_{2,527}(r_i)} \right)^2 \right) \right\}^{1/2}}{\sum_{r_i=H-35km}^{H-30km} \frac{X(r_i)_{PC,527}}{\beta_{2,527}(r_i) \cdot T_{527}^2(r_i)}} \tag{9}$$

and

$$\frac{\delta C_{PC,1053}}{C_{PC,1053}} = \left\{ \left( \frac{\delta C_{PC,527}}{C_{PC,527}} \right)^2 + \frac{\sum_{r_i=H-35km}^{H-30km} \left( \frac{X(r_i)_{PC,1053}}{T_{1053}^2(r_i)} \right)^2 \left( \frac{\delta X_{PC,1053}(r_i)}{X_{PC,1053}(r_i)} \right)^2}{n_0 \cdot \left( \sum_{r_i=H-35km}^{H-30km} \frac{X(r_i)_{PC,1053}}{T_{1053}^2(r_i)} \right)^2} + \frac{\sum_{r_i=H-35km}^{H-30km} \left( \frac{X(r_i)_{PC,527}}{T_{527}^2(r_i)} \right)^2 \left( \frac{\delta X_{PC,527}(r_i)}{X_{PC,527}(r_i)} \right)^2}{n_0 \cdot \left( \sum_{r_i=H-35km}^{H-30km} \frac{X(r_i)_{PC,527}}{T_{527}^2(r_i)} \right)^2} \right\}^{1/2} \tag{10}$$

Here only the uncertainties due to the detection noise and the uncertainties in molecular backscatter coefficient, i.e., the molecular density, were considered. The uncertainties due to the atmospheric optical transmissions at two wavelengths were not included because for the upper atmosphere the optical depths at these wavelengths are very small and therefore the transmission can be determined accurately. According to Elterman[23] the optical depth between the lidar (~ 550 km) and 30-35 km at 527 nm wavelength is ~ 0.001 due to the molecular scattering and < 0.003 due to ozone absorption. Hence, omitting both causes only an overestimation of < 0.4% for the atmospheric transmission. In practice the optical depth may vary due to changes in the ozone concentration, however, data of ozone distribution observed with other instruments can be used to calculate ozone absorption at 527 nm. At 1053 nm the optical depth in the upper atmosphere due to both ozone absorption and molecular scattering is negligible and the

atmospheric transmission between lidar and 30-35 km altitude can be set to 1.

The uncertainty in the molecular density at 30-35 km is 1-3 % over land.[22] It can be larger over oceans. This uncertainty effect to the determined lidar constant for the 527-nm PC channel. When regions are used for the calibration where precise molecular density data is available from other instruments, it may be possible to reduce this uncertainty to ~ 1%.

The uncertainties due to the detection noises can be decreased by integrating many laser shots (i.e., to increase $n0$). Calculations with Eqs. (9) and (10) show that by averaging 2000 laser shots, corresponding to 140 km horizontal distance, the uncertainty in the determined lidar constant is 2.4 % for the 527-nm PC channel and 56.3 % for the 1053 nm PC channel. If the average number is increased to $2x10^5$, corresponding to 14000 km in horizontal distance, the uncertainty for the 1053-nm PC channel can be reduced to ~ 5.6 %.

We also performed simulations of the ELISE calibration with noise-added lidar signals for comparison with estimations using Eqs. (9) and (10). The results are presented in Fig. 5(a) and 5(b). They show good agreement between the estimation and the simulation.

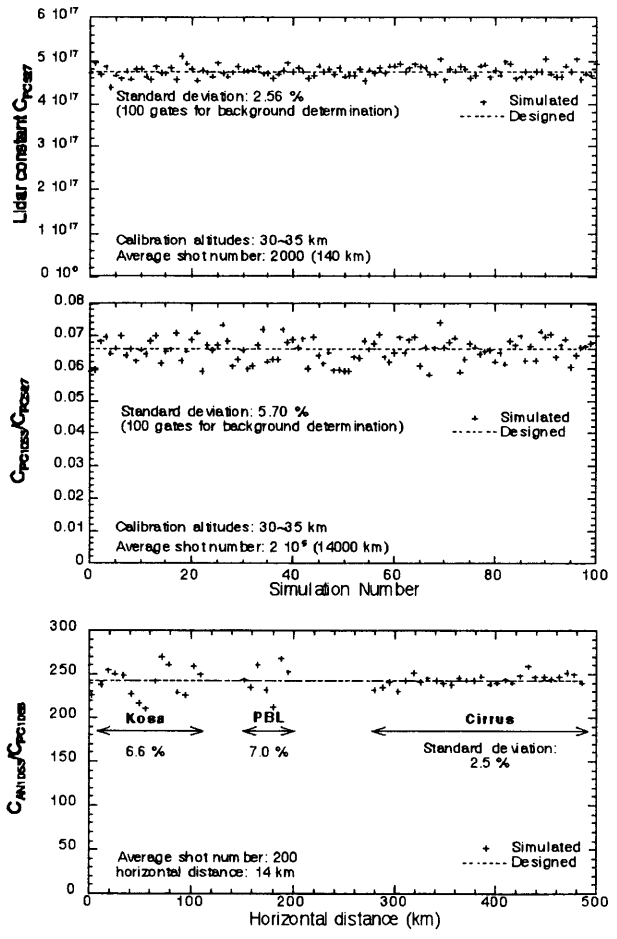


Figure 5 Simulation results for ELISE calibrations.

Figure 5(c) shows the ratio of lidar constants for the 1053-nm AN and PC channels determined using the signals from cirrus, Kosa and PBL aerosols shown in Fig. 2. The average shot number is 200 and the error ($1\sigma$) is 2.5%, 6.6% and 7.0%, respectively.

## 5. Method for Cloud Detection

In this section we describe the algorithm for detecting cloud top and base with ELISE. The top and base of clouds can be determined from the derivative of the lidar signal with respect to range or from the signal intensity itself by comparing it with a certain threshold.[24-26] Since the derivative algorithm is sensitive to the noise imposed on lidar return signals, it can be applied only to high SNR lidar signals. Therefore, the threshold algorithm is more suitable for cloud detection with ELISE.

The threshold algorithm compares measured lidar profiles with a reference lidar profile. If the measured lidar signal at an altitude is larger than the reference exceeding a threshold, $T_S$, then it is interpreted as cloud. The reference lidar profile either can be calculated from a standard atmosphere for each detection channel, or it can be defined from the observed data in clear atmospheric conditions. The threshold, $T_S$, must be determined according to the noise level. A low $T_S$ can increase the probability to detect optically thin clouds, but at the same time the probability of detecting false clouds due to noise is also increased. When assuming a Gaussian distribution for the noise with a standard deviation of $\sigma_n$ the threshold-to-noise ratio $TNR$ ($=T_S/\sigma_n$) determines the probability of noise exceeding $T_S$. This probability of false alarm is 2.3%, 0.14% and 0.005% when $TNR$ is set at 2, 3 and 4, respectively.[27] The ratio of $(N_C-T_S)/\sigma_n$ $=SNR-TNR$, ($N_C$ is the cloud signal level), defines the probability that the noise added cloud signal is less than $T_S$, i.e., the non-detection probability. Similarly, the non-detection probability is 2.3%, 0.14% and 0.005% when $SNR-TNR$ is equal to 2, 3 and 4, respectively. For ELISE cloud data analysis, we select a value of 2 for $TNR$ which may result in a noise false alarm probability of 2.3%, thus, the non-detection probability is less than 2.3% when $SNR$ is larger than 4.

The SNR is given by,

$$SNR = \frac{\sqrt{n_0} N_s}{\delta N} \quad . \qquad (11)$$

Where $n0$ is the number of laser shots integrated, $\delta N$ is given by Eqs.(3) and (5) for PC and AN detection,

respectively. From the condition $SNR > 4$ it is derived that the cloud top is detected when the backscatter coefficient at the cloud top is larger than

$$\beta_{t\,\min} = \frac{(H-r_t)^2}{CT^2(r_t)} \cdot \frac{1 + \sqrt{1 + 4\left[\delta N_{s,2}^2(r_t) + \delta N_b^2 + \delta N_d^2\right] \frac{n_0}{SNR^2}}}{2\frac{n_0}{SNR^2}} \qquad (12a)$$

for PC detection and

$$\beta_{t\,\min} = \frac{(H-r_t)^2}{CT^2(r_t)} \cdot \frac{F_m + \sqrt{F_m^2 + 4\left[\delta N_{s,2}^2(r_t) + \delta N_b^2 + \delta N_d^2\right] \frac{n_0}{SNR^2}}}{2\frac{n_0}{SNR^2}} \qquad (12b)$$

for AN detection. Here $T(r_t)$ is the transmission between the lidar and cloud top $r_t$. $\delta N_b$ and $\delta N_d$ have been calculated previously for each ELISE channel (see Table 3). $\delta N_{s,2(r_t)}$ is the noise due to the molecular scattering at the cloud top: $\delta N_{s,2(r_t)} = [N_{s,2(r_t)}]^{1/2}$ for PC detection and $\delta N_{s,2(r_t)} = [N_{s,2(r_t)} F_m]^{1/2}$ for AN detection, here $N_{s,2(r_t)}$ is the number of received molecular scattering and can be calculated from Eq.(1). Equations (12a) and (12b) can also be applied for estimating the detectable backscatter coefficient at the cloud base when range-dependent parameters are used for atmospheric transmission, etc. Assuming a rectangular, homogeneous cloud with a physical thickness of 1 km, we calculated the minimum cloud backscatter coefficients required to detect the cloud top and base using Eqs.(12a) and (12b) with $SNR$=4, respectively. Table 4 lists the results. We assumed that the typical altitudes of the cloud top of PSCs, cirrus and water clouds are 20 km, 10 km and 4 km, respectively.

Table 4 Minimum backscatter coefficients of a homogeneous cloud required to detect its top and base [a]

| | PC 527nm, night | | | PC 1053nm, night | | | AN 1053nm, night | | | AN 1053nm, day | | |
|---|---|---|---|---|---|---|---|---|---|---|---|---|
| Laser shots | 1 | 20 | 300 | 1 | 20 | 300 | 1 | 20 | 300 | 1 | 20 | 300 |
| Cloud top β ($m^{-1}sr^{-1}$) [b] | 1.1x10-5<br>1.2x10-5<br>1.2x10-5 | 6.4x10-7<br>9.0x10-7<br>1.1x10-6 | 8.9x10-8<br>1.6x10-8<br>2.3x10-7 | 1.6x10-4<br>1.7x10-4<br>1.7x10-4 | 8.0x10-6<br>8.3x10-6<br>8.5x10-6 | 5.4x10-7<br>5.9x10-7<br>6.3x10-7 | 3.2x10-5<br>3.3x10-5<br>3.4x10-5 | 6.2x10-6<br>6.5x10-6<br>6.6x10-6 | 1.6x10-6<br>1.7x10-6<br>1.7x10-6 | 4.1x10-5<br>4.3x10-5<br>4.4x10-5 | 8.4x10-6<br>8.7x10-6<br>8.9x10-6 | 2.1x10-6<br>2.2x10-6<br>2.2x10-6 |
| Cloud base β ($m^{-1}sr^{-1}$) [b] | - | 6.6x10-7<br>9.4x10-7<br>1.2x10-6 | 8.9x10-8<br>1.7x10-7<br>2.3x10-7 | - | 1.4x10-5<br>1.5x10-5<br>1.6x10-5 | 5.5x10-7<br>6.0x10-7<br>6.4x10-7 | - | 8.9x10-6<br>9.4x10-6<br>9.8x10-6 | 1.7x10-6<br>1.7x10-6<br>1.8x10-6 | - | 1.6x10-5<br>1.7x10-5<br>1.9x10-5 | 2.3x10-6<br>2.4x10-6<br>2.5x10-6 |
| Detectable cloud type [c] (top) | W Cl, Ci | W Cl, Ci, PSC $I_b$, II | W Cl, Ci, PSC $I_b$, II | W Cl | W Cl, Ci | W Cl, Ci, PSC II | W Cl | W Cl, Ci | W Cl, Ci | W Cl, Cl | W Cl, Ci | W Cl, Ci |

[a] Cloud physical thickness: 1 km; lidar ratio $S_t$=20 sr; vertical resolution: 100 m; TNR=2; SNR=4.

[b] Three value are given for the altitude of 20 km, 10 km and 4 km where PSC, cirrus and water clouds are assumed to typically exist, respectively.

[c] Ci: cirrus; W Cl: water cloud; PSC: polar stratospheric cloud.

It can be seen that for detection with the same average number of laser shots the backscatter coefficient at the cloud base has to be larger than at the cloud top because of the attenuation in the cloud. However, although a cloud with large backscatter coefficient can produce strong scattering signal, it also causes large attenuation of the laser pulse, resulting in the return signal smaller than $T_s$. For optically thick clouds, the cloud base detection can be more difficult because multiple scattering effects will lead to pulse stretching.

Comparing the detectable backscatter coefficients obtained from simulations and when using typical optical characteristics of clouds as listed in Table 2, we can draw the following conclusions:

(1) The tops of water clouds can be detected by all three detection channels even with a single laser shot. However, cloud base detection is not possible with a single shot.

(2) The cirrus top with the backscatter >$1.2\times10^{-5}$ ($m^{-1}sr^{-1}$) can be detected by the 527-nm PC channel with a single shot. Optically thin cirrus clouds can be detected by the 527-nm PC channel with 20 laser shots and by the 1053-nm PC and AN channels with 300 laser shots.

(3) Type $I_a$ PSCs cannot be detected even by the 527-nm PC channel with 300 laser shots (21-km horizontal resolution). Increasing the averaged number of shots is needed in order to detect this type of PSCs. The possibility for averaging will be limited, however, by the cloud horizontal scale. Type $I_b$ and II PSCs can be detected by the 527-nm PC channel with 20 laser shots, and by the 1053-nm PC channel with 300 laser shots.

(4) The ability to detect clouds with the 1053-nm AN channel is approximately the same for the nighttime and daytime observations, because the dark current is the dominant noise source.

Here we only considered a special case of single-layer cloud with homogeneous backscatter distribution. For realistic measurement, the cloud base detection depends on the backscatter coefficient at the base, the cloud optical depth, and the multiple scattering. For multi-layer clouds, the characteristics of the upper layer also influence the top detection of lower layers.

## 6. Retrievals of Optical Properties of Clouds and Aerosols

In this section, we apply various inversion algorithms to the simulated ELISE data in order to retrieve optical properties of clouds and aerosols.

A. Simple Two-Component Forward Method

Inversion algorithms which are based on solutions of the lidar equation are widely used to retrieve the backscatter or extinction profiles of aerosols and clouds from lidar return profiles. Two-component forward (near-end) and backward (far-end) solutions of the lidar equation were given by Fernald.[28] These solutions consider the scattering of aerosols and molecules separately, hence, they can provide accurate retrievals of backscatter (extinction) profiles of relatively clear atmospheres where molecular scattering cannot be neglected. Moreover, these solutions are useful when the boundary condition can be given at a range where aerosol scattering is negligible.

The near-end (forward integration) solution can be written as

$$\beta_1(r) = -\beta_2(r) + \frac{X(r)\exp[-2(S_1 - S_2)\int_{r_0}^{r}\beta_2(r')dr']}{CT^2(r_0) - 2S_1\int_{r_0}^{r}X(r')\exp[-2(S_1 - S_2)\int_{r_0}^{r'}\beta_2(r'')dr'']dr'} \quad (13)$$

Here $S_1$ is the aerosol lidar ratio; $S_2=8\pi/3$ is the molecular lidar ratio. $r_0$ is a reference range at the near end of the range interval under investigation. $T(r_0)$ is the transmission along the path from the lidar to $r_0$. The boundary condition term $CT^2(r_0)$ can be replaced by $X(r_0)/(\beta_1(r_0)+\beta_2(r_0))$. If $r_0$ can be located at a range where the aerosol scattering is sufficiently small compared to molecular scattering, the boundary condition can be determined easily by setting $\beta_1(r_0)$ to 0. For practical applications of Eq.(13), the aerosol lidar ratio $S_1$ must be known, too. The equation can directly be used to invert lidar return signals from the stratosphere where the aerosol lidar ratio can easily be determined from other measurements.

*1. Stratospheric Aerosol*

We applied Eq. (13) to the 527-nm and 1053-nm PC channels to retrieve stratospheric aerosol optical properties. To improve the SNR of the lidar profiles, signals were first smoothed by a sliding window with a vertical length of 300 m and a horizontal length of 14 km (200 shots) for 527-nm PC channel and 140 km (2000 shots) for 1053-nm PC channel. Then the lidar profile was inverted from 32 km to 12 km altitude with a constant lidar ratio of 50 sr. Note that the model atmosphere uses a modulating lidar ratio as shown in Fig. 2(b).

Figure 6 presents an example of retrieved backscatter (a) and extinction (b) profiles in the stratosphere at a horizontal distance of 560 km in the model atmosphere shown in Fig.2. As seen in Fig.6(b) the values of retrieved extinction profiles are smaller than in the original model, because the lidar ratio used in the inversion (50 sr) is smaller than the modeled value at 560 km (62.5 sr). However, better agreement can be seen in the retrieved backscatter profiles. This shows that the use of an assumed lidar ratio doesn't influence the retrieval of the backscatter coefficient in the stratosphere much because the optical thickness of stratospheric aerosols is small.

Figure 7 shows the derived integrated-backscatter-coefficient (IBC) at 527 nm and 1053 nm. The wave-like pattern in the retrieved 527-nm IBC is due to the use of constant lidar ratio in lidar signal inversions while the modeled lidar ratio is modulated. It can be seen in Fig. 7 that the IBC is not very sensitive to the assumption of the lidar ratio either. In addition, the wavelength dependence parameter of the backscatter coefficient for stratospheric

aerosol can be derived from the retrieved two-wavelength backscatter profiles, though it is not presented in this article.

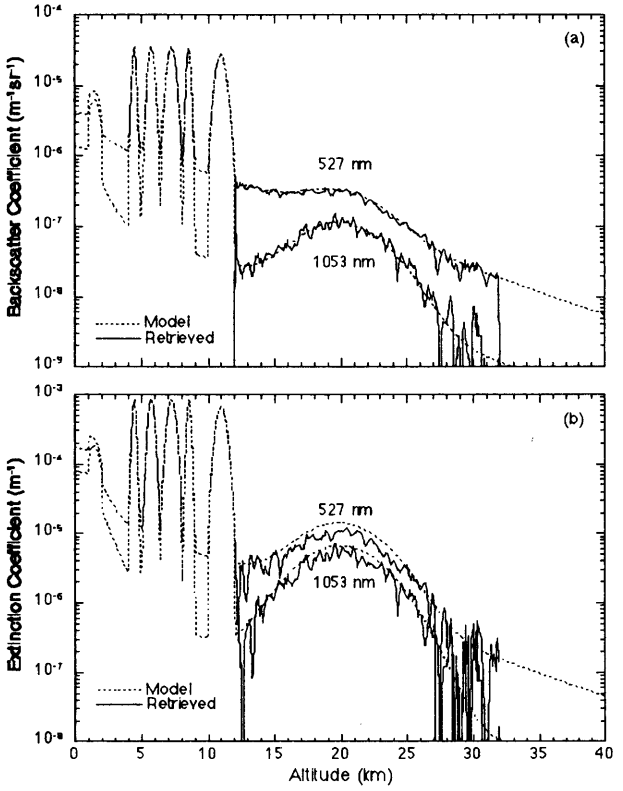


Figure 6 An example of retrieved stratospheric aerosol backscatter (a) and extinction (b) profiles at 560 km in the model atmosphere shown in Fig.2. The lidar signal inversion was initiated at 32 km altitude with Eq.(11).

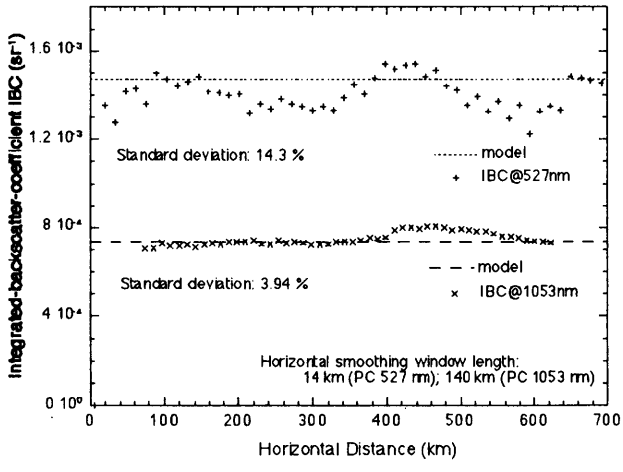


Figure 7 Retrieved integrated-backscatter-coefficient (IBC) for the stratosphere (from 13 to 30 km altitude) from the PC 527 nm and PC 1053 nm signals shown in Fig.3.

*2. Tropospheric Clouds and Aerosols*

After retrieving optical properties of aerosols in the stratosphere, we also simulated inversions of the 1053-nm PC and AN signals to retrieve backscatter (extinction) profiles of clouds and aerosols in the troposphere. The 527-nm PC signals were not used because of the saturation in cloud signals of this channel as demonstrated in Section 3B. Here the two-component solution as given in Eq. (13) was used again because the inversion also includes signals from aerosol layers in which the molecular scattering cannot be neglected. Figure 8 shows retrieved backscatter coefficients from the two 1053-nm channel signals for nighttime. The scale is the same as the one used in Fig.2. To improve the SNR lidar profiles were first smoothed horizontally by a sliding window with a width of 14 km before inverting them. The inversion was initiated at 12.5 km altitude with a constant lidar ratio of 20 sr for clouds and 50 sr for aerosols. The aerosol optical depths in the stratosphere, which can be derived from the retrieved IBCs as shown in Fig. 7, have been used in the inversion to account for transmission losses in the stratosphere. It becomes clear that backscatter coefficients near the far end of dense clouds cannot be retrieved since here the signal is already smaller than the noise level.

Figure 9 presents examples of the retrieved backscatter profiles at the horizontal distance of 70 km (a), 420 km (b) and 560 km (c). In each panel the solid line represents the model backscatter profile and the dashed and dotted lines indicate the backscatter profiles inverted from the signals for 1053-nm PC and AN channels. A cirrus layer between 10 and 12 km altitude with different optical depth and the PBL with a depth of 1.2 km are included in all three cases. Additionally a Kosa layer situated between 3 and 5 km in Fig.9(a), mid and low-altitude, multi-layer water clouds in Fig.(b) and (c) are assumed, respectively. Note the different scale in each panel: the scale in Fig.9(b) is 10 times larger than that in 9(c) and 100 times larger than that in 9(a).

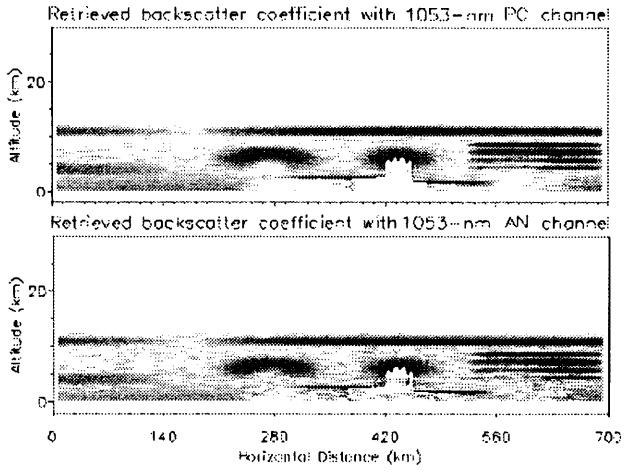


Fig. 8 Retrieved backscatter coefficient profiles from 1053-nm PC and AN channel signals using the two-component forward inversion [Eq.(11)]. The scale is the same as in Fig. 2.

As mentioned above constant lidar ratios were used both for clouds (20 sr) and aerosols (50 sr). These values are equal to the modeled values used in the signal generation at 70 km horizontal distance [see Fig. 2(b)]. Hence, the inversion reproduces the backscatter profile fairly well at this distance as can be seen in Fig.9(a). Relatively large variances are due to the small scattering (therefore low SNR). The used values of the lidar ratio in the inversion are 25% larger and lower than the model values at 420 and 560 km horizontal distances, respectively [also see Fig.2(b)]. As a consequence, over and underestimation are caused in the retrieved 420-km and 560-km backscatter profiles [Fig 9(b) and (c)], respectively. Moreover, the inversion of lidar signals at 420 km becomes unstable from about 5.4 km altitude. The cloud distribution below 5.4 km altitude can not be observed from the retrieved profiles, although the cloud structure can be recognized from the lidar signals (see Fig.3). Similar to the 420-km example, the inversion of 560-km signals is also unstable. As seen in Fig.9(c) the inverted backscatter profiles decrease quickly. The lowest cloud layer can therefore not be retrieved. This is connected to the generally unstable behavior of the forward inversion for the data analysis of optically thick clouds.[29]

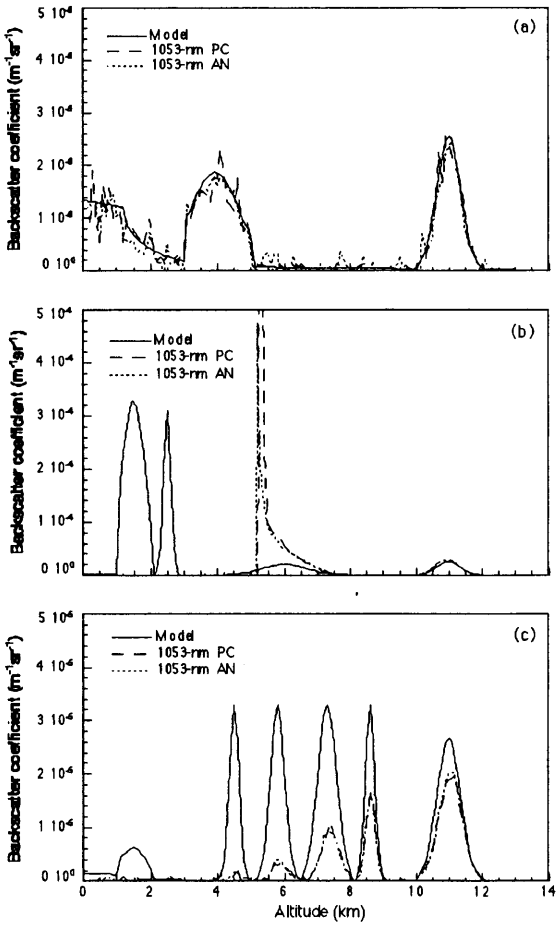


Fig. 9 Backscatter profiles at distance of 70 km (a), 420 km (b), and 560 km (c). Note different scales for backscatter coefficient.

As shown in above, an incorrect lidar ratio can cause large retrieval errors. The accurate determination of the lidar ratio is therefore required for the data analysis in clouds or optically thick aerosols in the troposphere. However, for cirrus clouds and tropospheric aerosols, the lidar ratio can vary over a large range, as discussed in Subsection 3A. Hence, in order to accurately deduce optical properties of cirrus clouds and aerosol methods are required which can determine the lidar ratio as well as the backscatter and extinction coefficients. In the following subsections we describe algorithms which can provide better retrievals of the cirrus and tropospheric aerosol optical properties and apply them to our simulated signals.

B. Algorithm for Cirrus

For the retrieval of cirrus optical properties we utilized an algorithm proposed by Young.[30] With this algorithm not only the backscatter profile but also the effective lidar ratio can be derived from lidar data with help of the cirrus optical depth. Consequently this method satisfies the requirement for the lidar ratio as discussed in the subsection above. Also, multiple scattering effects which are important in space-lidar measurements can be included.

Young extended the two-component solution to include a correction factor for multiple scattering. The algorithm uses the cloud optical depth as an extra boundary condition to retrieve cloud backscatter profiles. It can be formulated by two iterative equations:

$$\beta_1^{i+1}(r) = -\beta_2(r) + \frac{X(r)\exp[-2((\eta S_1)^i - S_2)\int_{r_t}^{r}\beta_2(r')dr']}{CT^2(r_t) - 2(\eta S_1)^i\int_{r_t}^{r}X(r')\exp[-2((\eta S_1)^i - S_2)\int_{r_t}^{r'}\beta_2(r'')dr'']dr'}; \quad (14a)$$

$$(\eta S_1)^{i+1} = \frac{\eta\tau_c}{\int_{r_t}^{r_b}\beta_1^{i+1}(r)dr}. \quad (14b)$$

Here $i$ is the number of iterations; $r_b$ and $r_t$ are the ranges from lidar to cloud base and top, respectively; $T(r_t)$ is the atmospheric transmission between the lidar and $r_t$; $\eta$ is a correction factor for multiple scattering. $\eta\tau_c$ is an effective cloud optical depth that is used as the extra boundary condition. It must be determined independently. It can be derived, for example, from molecular scattering signals above and below clouds or by comparing the cloud containing profile with a cloud-free reference profile.[30] $\eta S_1$ is an effective lidar ratio which can be determined simultaneously with the

backscatter profile. The far-end solution may be used by replacing (a) the boundary condition term in the denominator of Eq. (14a) with $CT^2(r_b)\exp[-2(\eta\tau_c+\tau_2)]$ and (b) the parameter $r_f$ in all other terms by $r_b$. The iteration can be initiated with $\eta S_f=0$. Only few iterations are required before the solution converges. Since we only considered single scattering, $\eta$ was actually set equal to 1 in our simulations.

We applied this method to our simulated data. The procedure is as follows: (1) The lidar profiles were smoothed by a horizontal sliding window with a width of 14 km. (2) The cirrus optical depths at different horizontal distances were derived from 527-nm PC profiles. This was done by comparing the cloud-free signals below the cirrus with the cirrus-free profile near 175 km horizontal distance in the atmospheric model shown in Fig.2. (3) The derived optical depths were then used as extra boundary conditions in order to iteratively invert cirrus profiles at 1053 nm using the far-end form of Eq. (14a). In that way, cirrus optical depths, lidar ratios, and backscatter profiles could be derived.

Figure 10 shows an example of the smoothed cirrus-free profile near 175 km and cirrus profile at 14 km horizontal distance. In the latter case the signals below the cirrus are smaller than those of the cirrus-free profile; this is due to the extinction in the cirrus. From the averaged ratio of these signals, the optical depth of cirrus was obtained. The derived (effective) optical depths and (effective) lidar ratios obtained with Young's method are shown in Fig. 11. When the cirrus optical depth is small (<0.25) significant relative errors are inherent in the retrieved optical depths and especially in the retrieved lidar ratios.

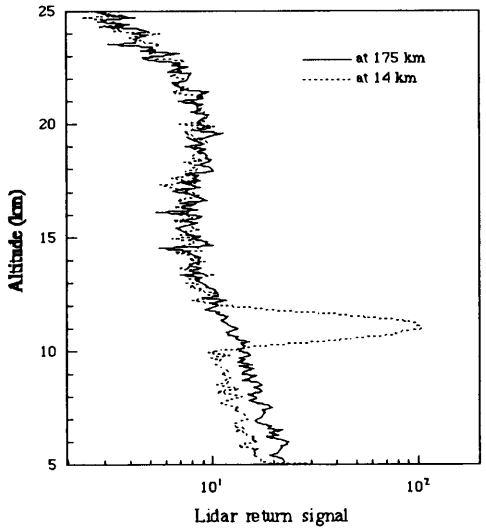


Fig. 10 Two lidar profiles of the PC 527 nm channel at 14 km and 175 km horizontal distances in the model atmosphere shown in Fig. 2. The cirrus optical depth can be derived by comparing the signals below 10 km in the cirrus profile at 14 km with those in the cirrus-free profile at 175 km.

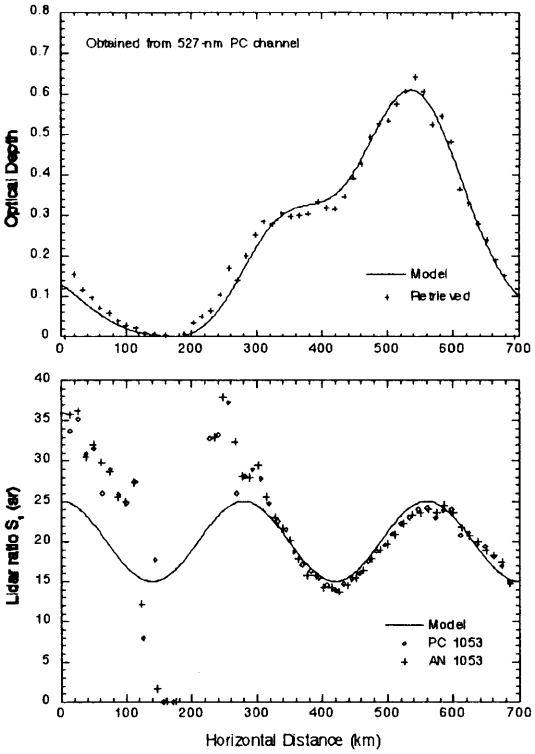


Fig. 11 Retrieved cirrus optical depths from the 527 nm PC channel signals (a), and lidar ratios from the 1053 nm PC and AN channel signals (b). Lidar profiles were smoothed by a sliding window with a width of 14 km.

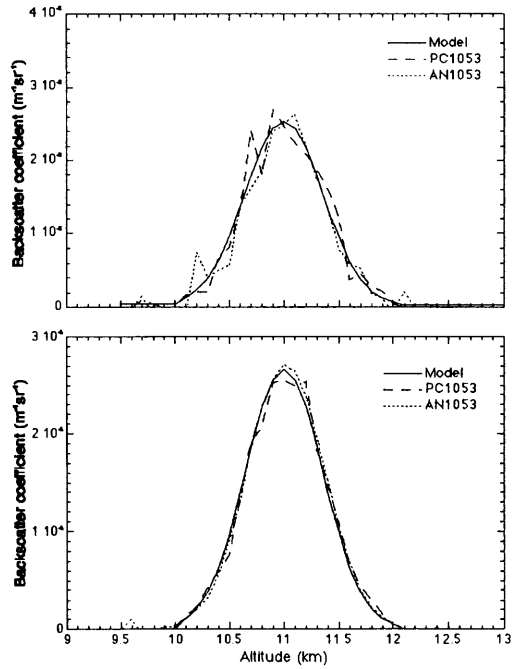


Fig. 12 Examples of retrieved backscatter profiles at 70 km (a) and 560 km (b). Note different scales for backscatter coefficient.

In Fig. 12 we applied Young's algorithm to the cirrus data analysis of the cases in Fig. 9(a) and (c). The retrieved profiles in the upper panel are similar to Fig.

9(a) where the correct lidar ratio was used for the inversion. The second example (lower panel) shows better reproductions of the backscatter profile than in Fig. 9(c). This demonstrates that Young's method considerably improves the inversion when the lidar ratio is uncertain.

C. Algorithm for Tropospheric Aerosols

We used a two-wavelength algorithm developed by Sasano and Browell [18] in the original and in a modified version for the retrieval of optical properties of tropospheric aerosols with PC 527-nm and 1053-nm signals. Sasano-Browell's method is based on the two-component lidar solution [Eq.(13)]. In addition, it assumes that aerosol size distribution and refractive index are invariant in the aerosol layer along the laser path, i.e., only the aerosol concentration changes. Hence, the backscatter profiles at different wavelengths are similar. Therefore, the retrieved two backscatter profiles at two wavelengths with true lidar ratios using Eq.(13) should also be similar and a so-called performance function should be minimum. The performance function is a measure of the degree of similarity. It is defined by

$$J(S_1) = \sum_{i=i_1}^{i_2} \left[ \frac{\beta_{1,S}(r_i)}{\beta_{2,S}(r_i)} - A \frac{\beta_{1,L}(r_i)}{\beta_{2,L}(r_i)} \right]^2, \qquad (15)$$

where subscripts $L$ and $S$ indicate the longer and shorter wavelength, respectively, $i1$ and $i2$ are the lower and upper limits for estimating the performance function, and $A$ is a proportionality constant. Because the lidar ratio is generally expected to have a value between 0 and 90 sr, the method uses 0 and 90 sr as a minimum and a maximum of the lidar ratio for the longer wavelength $S1,L$. Then, a smaller range of the lidar ratio for the shorter wavelength can correspondingly be determined. This is done by the following procedure. (1) Two backscatter profiles are calculated for the longer wavelength using Eq.(13) with the lidar ratio of 0 and 90 sr. (2) By tuning $S1,S$ and $A$ a number of backscatter profiles for the shorter wavelength are calculated with Eq. (13). Then, two sets of the performance function, $J(S1,S,A,S1,L=0)$ and $J(S1,S,A,S1,L=90)$, are derived. (3) A mapping procedure is applied to find the two combinations of $S1,S$ and $A$ which give the respective minima of $J(S1,S,A,S1,L=0)$ and $J(S1,S,A,S1,L=90)$.[18] In this way, two extremes of the lidar ratio for the shorter wavelength (minimum and maximum corresponding to $S1,L=0$ and 90 sr) can be determined. The range of the lidar ratio for the shorter wavelength defined by these two extremes is generally smaller than the assumed range for the longer-wavelength lidar ratio due to the wavelength dependence of the aerosol optical depth as discussed in the following. The true lidar ratio for the shorter-wavelength lies in the estimated range for $S1,S$.

The lidar ratio and the backscatter and extinction profiles at the short wavelength determined by this method have only small uncertainties when the aerosol optical depth at the longer wavelength is relatively small. The reason is that under this condition the retrieved two backscatter profiles at longer wavelength corresponding to the lidar ratios of 0 and 90 sr (i.e., without and with overestimated correction of attenuation due to aerosols) do not differ much, while the retrieval of the shorter-wavelength backscatter profile is sensitive to the lidar ratio due to the larger optical depth at this wavelength. To discuss this in more detail we simulated inversions using this method for a model aerosol. We considered a continental polluted type[19] which was homogeneously distributed in the PBL below an altitude of 1.5 km. The retrieved lidar ratio as a function of optical depth at the shorter wavelength is presented in Fig. 13. The optical depths at 527 nm and 1053 nm are different by a factor of 2 due to the assumption of a $\lambda^{-1}$ dependence of the extinction. It can be seen that the range of retrieved lidar ratio at 527 nm (shorter wavelength) is small when the aerosol optical depth is small. In this case the optical depth due to molecular scattering at shorter wavelength plays a key role (note that, the optical depths due to molecular scattering at 527 nm and 1053 nm are 16 times different).

However, as shown in Fig. 13, if the aerosol layer is optically thick, i.e., the aerosol optical depth is large at both shorter and longer wavelengths, the retrieved range of possible lidar ratios at the shorter wavelength is large because the inversion of longer-wavelength signal is also sensitive to the lidar ratio in this case. Hence, the method is limited to the analysis of optically thin aerosol layers.

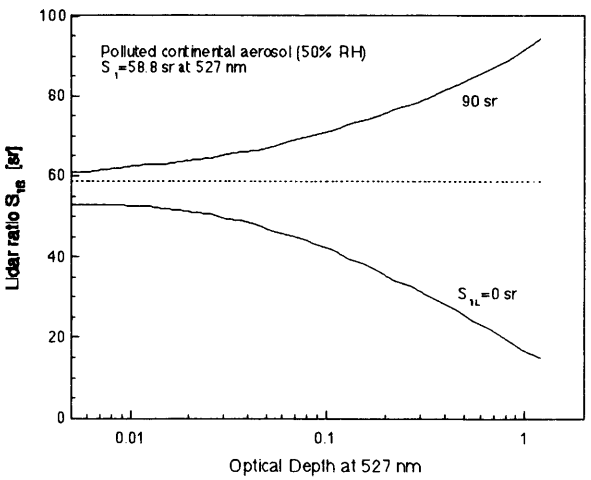


Fig. 13 Lidar ratio retrieved with Sasano-Browell's two-wavelength method as a function of optical depth at 527 nm for a model aerosol.

Therefore, we modified Sasano-Browell's algorithm for the analysis of signals from optically thick aerosols. The modified algorithm again assumes the similarity of the true backscatter profiles at different wavelengths and uses optionally Eq.(13) or its far-end form for the backscatter profile retrievals. A new performance function is defined by

$$J(S_{1,S}, S_{1,L}) = \frac{1}{(i_2 - i_1 + 1)} \sum_{i=i_1}^{i_2} \left[ \frac{\beta_{1,S}(r_i)}{\beta_{1,L}(r_i)} - \frac{1}{(i_2 - i_1 + 1)} \sum_{i=i_1}^{i_2} \frac{\beta_{1,S}(r_i)}{\beta_{1,L}(r_i)} \right]^2 . \quad (16)$$

This new function does not include the proportionality constant $A$ which was used in Eq.(15). Hence, the mapping procedure is no longer necessary when the modified version of Sasano-Browell's algorithm is used. Since in the case of optically thick aerosols the inversions at both shorter and longer wavelength are sensitive to the lidar ratio, $S_{1,L}$ is scanned in the modified algorithm in the same way between 0 and 90 sr as $S_{1,S}$. $S_{1,L}$ and $S_{1,S}$ are determined by minimizing Eq. (16). The boundary condition in the lidar equation solutions can be determined with a matching technique that calibrates lidar profiles with an aerosol-free layer. Also, $CT^2(r_f)$ can be used as a constrain when the lidar system can be calibrated absolutely as in ELISE.

Both methods can provide simultaneous retrievals of the lidar ratio and the backscatter profile of aerosols. As an additional parameter, the wavelength dependence parameter can be determined after retrieving the backscatter profiles at longer and shorter wavelengths. However, both methods assume the similarity of aerosol backscatter profiles at different wavelengths as described above. For real atmospheres this requirement is not likely to be satisfied. Therefore, large errors can be caused in retrievals with these methods.

We tested the possibilities of the data analysis using both two-wavelength methods with simulated lidar signals. Before applying them, simulated lidar profiles were smoothed by a sliding window with a width of 300 m in altitude and 56 km (400 shots) in horizontal distance to improve the SNR. Figure 14 presents retrieved lidar ratios of the Kosa layer at 3-5 km altitudes and 0-100 km distances in the model of Fig. 2. Eq.(13) was used for the 1053-nm PC signal inversion. For the 527-nm PC signal inversion, the boundary condition was used in the form $X(r_0)/(\beta_1(r_0)+\beta_2(r_0))$ because the molecular scattering signals between the Kosa layer and the cirrus are available in the 527-nm PC channel. Both $S_{1L}$ and $S_{1S}$ were changed from 0 sr to 90 sr with increments of 1 sr. Figure 14 reveals that the range of possible $S_{1S}$ determined by Sasano-Browell's method is smaller than 25 sr. This is much smaller than the assumed values for 1053 nm (90 sr). If the SNR is high the retrieval of $S_{1S}$ can be further improved by using the modified algorithm which we described above. The variations for the retrieved $S_{1L}$ are relatively large. This is mainly due to the low SNR of the PC 1053 nm signal. Our simulations showed that two-wavelength algorithms are very sensitive to detection noise. High SNR is therefore required when applying a two-wavelength inversion algorithm. This can only be achieved by integrating a large number of lidar profiles provided that the horizontal extension of the aerosol layer is large enough.

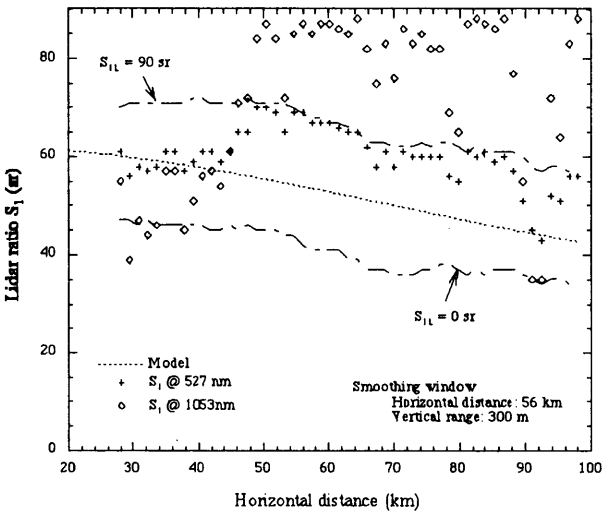


Fig. 14 Two wavelength data analysis of Kosa layer at 3-5 km altitudes and 0-100 km horizontal distances.

## 7. Effects of Cloud Inhomogeneity

Spatial inhomogeneity of clouds may produce large errors in the retrieval of cloud structures and optical properties from space lidar measurements when many lidar profiles are averaged in order to get a high SNR.[31] This is due to the high ground speed of spaceborne lidars, which results in large distance between the centers of individual footprints. In this section, we discuss some problems related to the retrieval of cloud optical properties from averaged lidar profiles.

With the correction of multiple scattering within clouds, the integrated lidar return signal can be written as

$$N(r) = \frac{CT_0^2}{r^2} \sum_{j=1}^{n_0} \left( \beta_{1j}(r) + \beta_2(r) \right) \exp\left( -2 \int_{r_0}^{r} \left[ \eta_j(r') \sigma_{1j}(r') + \sigma_2(r') \right] dr' \right) , \quad (17)$$

where $n_0$ is the integration number of laser shots, $T_0$ is

the atmospheric transmission from lidar to $r_0$, $\eta_j(r)$ is the multiple scattering correction factor for $j^{th}$ lidar profile.

If the cloud structure is variable along the lidar track, the cloud top height determined with the threshold method is the height for which the averaged signal is higher than *TNR*. The cloud base can be detected similarly. Assume a situation where a number of laser shots is averaged and only a part of them hits a cloud. If the averaged cloud signal is larger than *TNR*, then it is interpreted as a cloud extending over the full distance of the average. This will result in an overestimation of cloud cover rate. On the other side, if the averaged cloud signal is smaller than *TNR* the cloud cannot be detected. That would result in an underestimation of cloud cover rate. Hence, the beam-filling problem as faced by most conventional spaceborne remote sensing instruments[32] may still be important for space lidars when a number of laser shots is averaged.

The cloud inhomogeneity also influences retrievals of cloud optical properties. In the following we will discuss this problem in more detail. Eq. (17) can be rewritten as

$$N(r) = \frac{n_0 \cdot C \cdot T_0^2}{r^2}\left[\beta_{1,eff}(r) + \beta_2(r)\right] \cdot T^2(r), \tag{18}$$

where

$$\beta_{1,eff}(r) = \frac{\sum_{i=1}^{n_0} \beta_{1,j}(r')T_{1,j}^2(r)}{\sum_{i=1}^{n_0} T_{1,j}^2(r)} = \frac{\sum_{i=1}^{n_0} \beta_{1,j}(r') \exp\left(-2\int_{r_0}^{r} \eta_j(r')\sigma_{1,j}(r')dr'\right)}{\sum_{i=1}^{n_0} \exp\left(-2\int_{r_0}^{r} \eta_j(r')\sigma_{1,j}(r')dr'\right)} \tag{19}$$

is an effective backscatter coefficient, and

$$T^2(r) = \frac{1}{n_0}\sum_{i=1}^{n_0} T_j^2(r) = \frac{1}{n_0}\sum_{i=1}^{n_0} \exp\left(-2\int_{r_0}^{r}\left[\eta_j(r')\sigma_{1,j}(r') + \sigma_2(r')\right]dr'\right) \tag{20}$$

is the mean transmission; $r_0$ is a range above the cloud. We introduce a new effective lidar ratio into Eq.(18) given by

$$S_{1,eff}(r) = \frac{\sigma_{1,eff}(r)}{\beta_{1,eff}(r)}, \tag{21}$$

where

$$\sigma_{1,eff}(r) = \frac{1}{2}\frac{d}{dr}\ln\left[T^2(r)\right] - \sigma_2(r) \tag{22}$$

is an effective extinction coefficient derived from the averaged lidar profile. Since Eq.(18) has the same form as the conventional single-shot lidar equation, it can be solved similarly. Then the near-end solution can be derived. It is given by

$$\beta_{1,eff}(r) = -\beta_2(r) + \frac{X(r)\exp\left[-2\int_{r_0}^{r}(S_{1,eff}(r'') - S_2)\beta_2(r')dr'\right]}{CT^2(r_0) - 2\int_{r_0}^{r} S_{1,eff}(r')X(r')\exp\left[-2\int_{r_0}^{r'}(S_{1,eff}(r'') - S_2)\beta_2(r'')dr''\right]dr'} \tag{23}$$

Here, the effective lidar ratio was treated as a variable with range. Assuming a constant effective lidar ratio, Eq. (23) obtains the same form as the near-end solution of the single-shot lidar equation [Eq.(13)]. This indicates that algorithms based on Eq.(13) or its modified form including the multiple scattering can be used to invert the averaged lidar profile. However, only the effective backscatter, extinction and lidar ratio represented by Eqs. (19), (21) and (22), respectively, can be retrieved. Here, the retrieved backscatter is a mean weighted by the cloud transmissions.

Figure 15 presents examples which show the effect of cloud inhomogeneity on cloud measurements. A rectangularly distributed cloud was assumed [Fig. 15(a)] and multiple scattering was neglected. Two cases of the cloud backscatter coefficient were considered; one is $1\times10^{-5}$ $m^{-1}sr^{-1}$ which is a typical value of cirrus clouds, and the other is $5\times10^{-4}$ $m^{-1}sr^{-1}$ as an example of a water cloud. The far-end two-component solution was used for the inversion. For both cases, the retrieved backscatter coefficients [Fig. 15(b) and 15(c)] at the cloud top are equal to the means of the cloud backscatter coefficients according to Eq. (19), i.e., $\beta_C n_1/n_0$ provided that $\beta_C$ is the cloud backscatter coefficient. They decrease with the depth in cloud at different rates. For the case of optically thin cloud (cirrus), the retrieved backscatter coefficients decrease slowly [Fig. 15(b)] and the cloud base detection is possible. However, for the case of optically thick

cloud, even if only one pulse does not hit the cloud, the retrieved backscatter profile quickly approaches zero. Retrieval of the backscatter profile and detection of the cloud base is not possible in this case. In principle the decreasing behavior of the retrieved backscatter coefficient can be described by Eq. (19). However, the denser the cloud is and the larger the depth in cloud is, the smaller the cloud transmission will be. Therefore, the weighting of the cloud transmission in Eq. (19) becomes less significant.

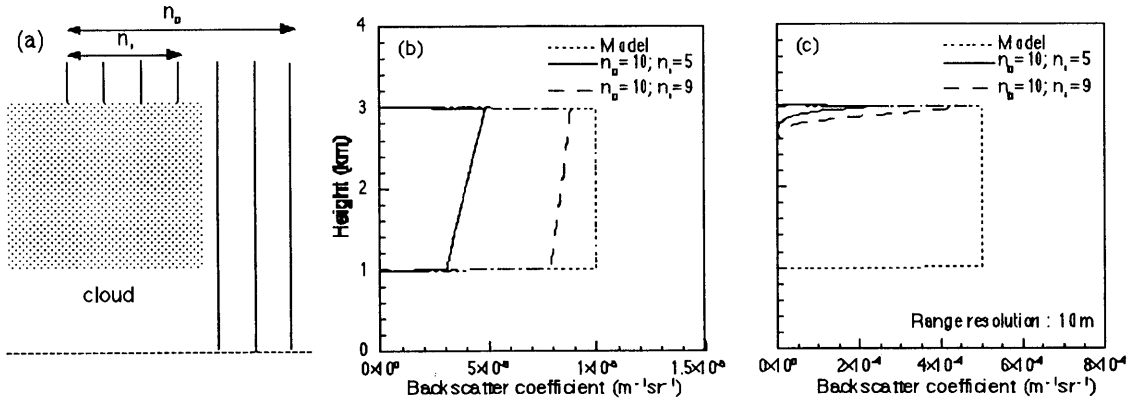


Fig. 15 An example of simulations for the effect of cloud inhomogeneity on cloud optical property retrievals from averaged lidar profiles. n0 represents the average number of laser shots and n1 represents the number of laser shots that hit the cloud. (b) shows an optically thin case, (c) an optically thick case.

When the multiple scattering is negligibly small (i.e., $\eta \approx 1$) as in the case of ground-based lidar with small receiver FOV, and additionally the cloud lidar ratio is constant, then the true lidar ratio can be retrieved from averaged lidar profiles. This can be shown by using the relation

$$-\frac{d}{dr}\ln\left[T^2(r)\right] = \frac{1}{T^2(r)}\frac{d}{dr}T^2(r) = -\frac{2}{n_0 T^2(r)}\sum_{i=1}^{n_0}\left[\sigma_{1,j}(r)+\sigma_2(r)\right]T_j^2(r)$$

$$= -2S_{1,0}\beta_{1,eff}(r) - 2\sigma_2(r) \quad , \qquad (24)$$

where $S_{1,0}$ represents the true cloud lidar ratio. Our simulations of the lidar ratio retrieval validated this conclusion.

With the analytical equations Eqs. (19) to (21) one can directly assess the reliability of retrievals of optical properties of inhomogeneously distributed clouds when using the averaged lidar profile in the data analysis. Neither cloud backscatter profile nor cloud extinction profile can be correctly retrieved from the averaged lidar profile. However, the cloud lidar ratio can be retrieved when it is constant and multiple scattering is negligible.

## 8. Conclusions

We discussed data analysis methods and presented simulations for measurements of clouds and aerosols with ELISE. Simulation results showed that ELISE can observe not only the structure of clouds and distribution patterns of aerosols but can also yield quantitative optical properties of aerosols and clouds.

In the cloud detection, the cloud top of most clouds, namely, cirrus, water clouds, and Type $I_b$ and Type II PSCs can be detected. For stratospheric aerosols, the backscatter profile can be retrieved when assuming a lidar ratio. For cirrus observations, backscatter profile, effective optical depth and lidar ratio can be derived. In the case of tropospheric dust layers, the two-wavelength method can be used to obtain backscatter and extinction profiles, lidar ratios and wavelength dependence parameters when the aerosol layer extends over a sufficiently large range.

We also discussed the problem of cloud inhomogeneity effects on cloud measurements with spaceborne lidars. Analytical equations were given with which one can easily analyze the retrieval of optical properties of inhomogeneously distributed clouds from the averaged lidar profiles. It is shown that the inversion algorithms for the single-shot lidar signal can be applied to analyze the averaged lidar profile. However, only the mean backscatter profile weighted by cloud transmissions can be retrieved. Simulation examples showed very large effects of the cloud inhomogeneity on both backscatter retrieval and cloud base determination in dense clouds

when a number of lidar profiles is averaged and inverted. For optically thin clouds (cirrus), the effect is relatively small and cloud base detection is possible.

**Acknowledgments**

This work was funded by the Global Environment Research Fund of the Environmental Agency of Japan. The ELISE project has been conducted by the National Space Development Agency of Japan. The authors thank Yasuhiro Sasano, Yasuaki Kawamura, Kenji Tatsumi and Tadashi Imai for useful discussion.

**References:**

1. R. D. Cess, G. L. Potter, J. P. Blanchet, G. J. Boer, A. D. D. Genio, M. Deque, V. Dymnikov, V. Galin, W. L. Gates, S. J. Ghan, J. T. Kiehl, A. A. Lacis, H. L. Treut, Z. X. Li, X. Z. Liang, B. J. McAvaney, V. P. Meleshko, J. F. B. Mitchell, J. J. Morcrette, D. A. Randall, L. Rikus, E. Roeckner, J. F. Royer, U. Schlese, D. A. Sheinin, A. Slingo, A. P. Sokolov, K. E. Taylor, W. M. Washington, R. T. Wetherald, I. Yagai, and M. H. Zhang, "Intercomparison and interpretation of climate feedback processes in 19 atmospheric general circulation models," *J. Geophys. Res.*, **95**, 16,601-16,615 (1990).
2. D. M. Winker, R. H. Couch, and M. P. McCormick, "An overview of LITE: NASA's Lidar In-space Technology Experiment," *Proc. IEEE*, **84**, 164-179 (1996).
3. T. Imai, Y. Kawamura, N. Tanioka, K. Asai, T. Itabe, O. Uchino, T. Kobayashi, Y. Sasano, and T. Aoyagi, "NASDA ELISE (MDS-LIDAR) Program," *Proc. of SPIE*, **3218**, 177-183 (1997).
4. Y. Sasano, K. Asai, N. Sugimoto, Y. Kawamura, K. Tatsumi, and T. Imai, "NASDA Mission Demonstration Satellite lidar project and its sciences," *Proc. SPIE*, **3504**, 2-7 (1998).
5. C. M. R. Platt, "Remote sounding of high clouds, VI, Optical properties of midlatitude and tropical cirrus,"*J. Atmos. Sci.*, **44**, 729-747 (1987).
6. A. Notari, U. N. Singh, T. D. Wilkerson, and W. C. Braun, "Optical properties of high clouds, Optical remote sensing of the atmosphere," *Tech.Dig.Ser.*, **4**, 210-212 (1990).
7. A. Ansmann, J. Bosenberg, G. Brogniez, S. Elouragini, P. H. Flamant, K. Klapheck, H. Linne, L. Menenger, W. Michaelis, M. Riebesell, C. Senff, P.-Y. Thro, U. Wandinger, and C. Weitkamp, "Lidar network observations of cirrus morphological and scattering properties during the International Cirrus Experiment 1989: The 18 October 1989 case study and statistical analysis," *J. Appl.Meteorol.*, **32**, 1608-1622 (1993).
8. D. G. Guasta, M. Morandi, and L. Stefanutti, "One year of cloud lidar data from Dumont d'Urville (Antarctica) 1. General overview of geometrical and optical properties," *J. Geophys. Res.*, **98**, 18,575-18,587 (1993).
9. Y. Takano and K.-N. Liou, "Solar radiative transfer in cirrus clouds. Part I: Single scattering and Optical Properties of Hexagonal Ice Crystals,"*J. Atmos.Sci.*, **46**, 818-837 (1989).
10. Y. Takano and K.-N. Liou, "Radiative transfer in cirrus clouds. Part III: Light scattering by irregular ice crystals," *J. Atmos.Sci.*, **52**, 3-19 (1995).
11. R. G. Pinnick, S. G. Jennings, P. Chylek, C. Ham, and W. T. Grandy, Jr., "Backscatter and Extinction in Water Clouds," *J. Geophys. Res.*, **88**, 6787-6796 (1983).
12. V. E. Derr, "Estimation of the extinction coefficient of clouds from multiwavelength lidar backscatter measurements," *Appl. Opt.*, **19**, 2310-2314 (1980).
13. L. R. Poole, M. T. Osborn, and Q. H. Hunt, 1988, "Lidar observations of arctic polar stratospheric clouds, 1988: Signature of small, solid particles above the frost point," *Geophys. Res. Lett.*, **15**, 867-870 (1988).
14. E. V. Browell, C. F. Butler, S. Ismail, P. A. Robinette, A. F. Carter, N. S. higdon, O. B. Toon M. R. Schoeberl, and A. F. Tuck, "Airborne lidar observations in the wintertime Arctic Stratosphere: 1. Polar stratospheric clouds," *Geophys. Res. Lett.*, **17**, 385-388 (1990).
15. H. Jaeger and D. Hofmann, "Midlatitude lidar backscatter to mass, area, and extinction conversion model based in situ aerosol measurements from 1980 to 1987," *Appl. Opt.*, **30**, 127-138 (1991).
16. G. P. Gobbi, "Lidar estimation of stratospheric aerosol properties: Surface, volume, and extinction to backscatter ratio," *J. Geophys. Res.*, **100**, 11,219-11,235 (1995).
17. K. Parameswaran, K. O. Rose, and B. V. K. Murthy, "Relationship between backscattering and extinction coefficients of aerosols with application to turbid atmosphere,"*Appl. Opt.*, **30**, 3059-3071 (1991).
18. Y. Sasano and E. V. Browell, "Light scattering characteristics of various aerosol types derived from multiple wavelength lidar observations," *Appl. Opt.*, **28**, 1670-1679 (1989).
19. M. Hess, P. Koepke, and I. Schult, "Optical Properties of Aerosols and Clouds: The Software Package OPAC," *Bull. Am. Meteor. Soc.*, **79**, 831-844 (1998).
20. T. Nakajima, M. Tanaka, M. Yamano, M. Shiobara, K. Arao, and Y. Nakanishi, "Aerosol optical characteristics in the yellow sand events observed in May, 1982 at Nagasaki - Part II models," *J. Meteor. Soc. Jpn.*, **67**, 279-291 (1989).
21. P. P. Webb, R. J. McIntyre, and J. Conradi, "Properties of avalanche photo-diodes," RCA Rev. 35, 234-278 (1974).
22. P. B. Russell, B. M. Morley, J. M. Livingston, G. W. Grams, and E. M. Patterson, "Orbiting lidar simulations. 1: Aerosol and cloud measurements by

an independent-wavelength technique," *Appl. Opt.*, **21**, 1541-1553 (1982).
23. L. Elterman, L., "UV, visible, and IR attenuation for altitudes to 50 km, 1968," Environmental Research Papers, No. 285, Air Force Cambridge Research Laboratories, Bedford, Massachusetts (1968).
24. K. Sassen and B. S. Cho, "Subvisual-thin cirrus lidar dataset for satellite verification and climatological research," *J. Appl. Meteorol.*, **31**, 1275-1285 (1972).
25. S. R. Pal, W. Steinbrecht, and A. I. Carswell, " Automated method for lidar determination of cloud base height and vertical extent," *Appl. Opt.*, **31**, 1488-1494 (1992).
26. C. M. R. Platt, S. A. Young, A. I. Carswell, S. R. Pal, M. P. McCormick, D. . Winker, M. D. Guasta, L. Stefanutti, W. L., Eberhard, R. M. Hardesty, P. H. Flamant, R. Valentin, B. Forgan, G. G. Gimmestad, H. Jager, S. S. Khmelevtsov, I. Kolev, B. Kaprielov, D-R. Lu, K. Sassen, V. S. Shamanaev, O. Uchino, Y. Mizuno, U. Wandinger, C. Weitkamp, A. Ansmann, and C. Wooldridge, "The Experimental Cloud Lidar Pilot Study (ECLIPS) for cloud-radiation research," *Bull. Am. Meteorol. Soc.*, **75**, 1634-1654 (1994).
27. J. M. Pelon, Desbois, P. H. Flamant, H. L. Treut, G. Seze, M. Doutriaux, V. Trouillet, P. Chazette, S. Elouragini, C. Glamant, F. Lieutaud, J.-L. Raffaelli, and R. Valentin, "A study of the potential contribution of a backscatter lidar to climatological studies," Final Report, contract AO/1-2668/92/NL/CN of the European Space Research and Technology Center (ESTEC), Noordwijk, Netherlands (1996).
28. F. G. Fernald, F.G., "Analysis of atmospheric lidar observations: some comments," *Appl. Opt.*, **23**, 652-653 (1984).
29. J. D. Klett,"Stable analytical inversion solution for processing lidar returns," *Appl. Opt.*, **20**, 211-220 (1984).
30. S. A. Young, S.A., "Analysis of lidar backscatter profiles in optically thin clouds," *Appl. Opt.*, **34**, 7019-7031 (1995).
31. Z. Liu and N. Sugimoto, "Theoretical and experimental study of inversion algorithms for space lidar observation of clouds and aerosols," *Proc. of SPIE*, **3494**, 296-305 (1998).
32. B. A. Wielicki and L. Parker, "On the determination of cloud cover from satellite sensors: The effect of sensor spatial resolution,"*J. Geophys. Res.*, **97**, 12,799-12,823 (1992).

# Effects of Multiple Scattering on the Retrieval of Optical Parameters from ELISE - Simulation Study

Peter Völger, Zhaoyan Liu, and Nobuo Sugimoto

National Institute for Environmental Studies, 16-2 Onogawa, Tsukuba, 305-0053, Japan

## ABSTRACT

We present results from a study investigating the influence of multiple scattering effects on measurements with ELISE, a new spaceborne lidar to be launched in 2002. The influence of the multiple scattering portion of the total detected signal on measurements of aerosols in the Planetary Boundary Layer is discussed.

**Keywords:** Spaceborne lidar, multiple scattering

## 1. INTRODUCTION

One of the main difficulties in improving predictions of future climate is the problem of improving the quality of input data. Today's General Circulation Models (GCMs) rely to a large extend on observation data from satellite-borne passive remote sensing instruments. While this allows for information with global coverage the height resolution is rather poor. Additionally, optically thin atmospheric objects tend to be invisible for these instruments. In recent decades ground-based and airborne lidars have proved to be able to provide atmospheric data with good height resolution. A first spaceborne lidar experiment performed by NASA (LITE) in 1994 showed that such lidar systems are also capable to provide information with both excellent vertical and horizontal resolution.[1]

Currently Japan's National Space Development Agency (NASDA) is developing a new lidar system for space application. The so-called "Experimental Lidar in Space Equipment" (ELISE for short) is scheduled to be launched in 2002 as part of NASDA's Mission Demonstration Satellite 2. The goals are (a) to demonstrate the applicability of the lidar's key componentents for long-term operation in space and (b) to provide observation data with almost global coverage over one year period. The observations aim mainly at detecting boundaries of optically thin clouds and aerosol layers, estimating their optical thickness and investigating multi-layered cloud systems.

It is well known that multiple scattering effects contribute significantly to backscatter signals detected from spaceborne lidar systems.[1,2] However, for a given atmosphere the exact portion of multiple scattering intensities depends on the system parameters, mainly the field-of-view and the distance between lidar and layer under investigation. Other variables might also affect the signal inversion. Hence, multiple scattering estimates for different lidar characteristics cannot be applied to measurements with ELISE.

The influence of multiple scattering on measurements with ELISE is currently subject of a detailed investigation. In the following we will report some findings from our study concerning the impact of multiple scattering on measurements of aerosols in the Planetary Boundary Layer (PBL).

## 2. SPECIFICATIONS OF ELISE

ELISE's system parameters were already published and discussed in detail elsewhere (see e.g. Ref. 3). They shall only briefly be introduced here. ELISE will be a backscatter lidar with two wavelengths, 1053 and 527nm. The backscatter signal will be detected both in photon counting mode (at both wavelengths) and in analog mode (only at 1053nm). The direction of the measurements is planned to be nadir-looking. Footprints will be overlapping with a distance of about 70m between their centers. However, for the data collection an integration over 20 shots is intended, reducing the horizontal resolution to 1.4km. In the vertical measurements will cover the range between 0 and 35km altitude with a height resolution of 100m. Due to the orbital parameters ELISE's measurements will nearly cover the whole globe. A summary of the major specifications is given in Table 1.

Send correspondence to peter.voelger@nies.go.jp

Part of the EUROPTO Conference on Laser Radar Ranging and Atmospheric Lidar Techniques II
Florence, Italy • September 1999
SPIE Vol. 3865 • 0277-786X/99/$10.00

**Table 1.** ELISE major specifications (design)

| | |
|---|---|
| Satellite | |
| Orbit | circular (sun-synchronous) |
| Height | ca. 550km |
| Inclination angle | 97.59° |
| Ground speed | 6.983km/s |
| Period | 95.6min |
| Transmitter | |
| Laser | LD pumped Nd:YLF |
| Output energy | 84mJ @ 1053nm; 10mJ @ 527nm |
| Pulse repetition rate | 100Hz |
| Beam divergence | 0.17mrad (FWHM) |
| Receiver | |
| Effective Diameter | 1m |
| Field of view | 0.21mrad (full angle) |
| Detectors | APD |
| Detection mode | 1x Analog @ 1053nm |
| | 2x Photon counting (@ 527 and 1053nm) |
| Measurement | |
| Direction | Nadir |
| Height coverage | 0–35km |
| Vertical resolution | 100m |
| Horizontal resolution | 1.4km (Integration 20 shots) |

## 3. SIMULATIONS

The geometry for space lidar measurements differs significantly from common lidar applications like ground-based or airborne systems since the objects of observation are in a much larger distance. Consequently, the footprint of both laser and receiver, and therefore also the observed volume in each rangebin, will be larger. For this reason it can be expected that multiple scattering will play a more important role than in other, more common lidar geometries. Also multiple scattering estimates for other spaceborne lidar systems as LITE cannot be applied to ELISE's measurements, as multiple scattering intensities are largely influenced by the specifications of the individual lidar system. An example for a comparison of ratios of multiple to single scattering for LITE and ELISE is shown in Fig. 1. A simple case of an aerosol layer between 0 and 2km altitude which consisted of a continental polluted aerosol mixture[4] with an extinction coefficient of $0.5\text{km}^{-1}$ was considered. In this example the relative contribution to the detected signal is for LITE almost three times as high as for ELISE despite the shorter distance to the layer. The reason is LITE's larger FOV. However, the differences vary with the atmospheric constituent, indicating the dependence on the phase function of the layer.

Our study consists basically of two steps. First, lidar signals including multiple scattering intensities have to be generated. This is done by using a Monte Carlo model which was developed at the University of Munich.[5,6] The model calculates both the total backscatter intensity and the intensities of the individual scattering orders. However, though simulations of lidar returns can give us some information about the influence of multiple scattering on the total backscatter signal, this information is only of limited practical use. Therefore, in a second step, the aim must be to estimate the impact of multiple scattering intensities on the retrieval of optical parameters from the lidar signal. A simple, approximative way to include multiple scattering effects in the commonly used lidar equation was proposed by Kunkel and Weinman.[7] They introduced a factor $F$ and modified the lidar equation to

$$P_T(R) = C\frac{1}{R^2}\beta(R)\exp\left(-2[1-F(R)]\int_0^R \sigma(r)dr\right). \quad (1)$$

Here $P_T(R)$ is the total received signal from distance $R$, $C$ is the system constant, and $\sigma$ and $\beta$ are the extinction

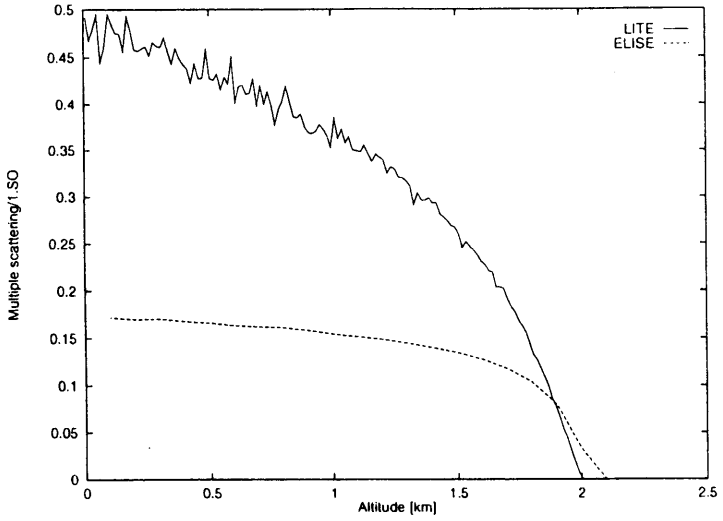


**Figure 1.** Multiple to single scattering ratio for an aerosol layer between 0 and 2km altitude consisting of a continental polluted type. The extinction coefficient is $0.5\text{km}^{-1}$.

and backscatter coefficient, respectively. The multiple scattering factor can be calculated according to

$$F(R) = \frac{1}{2\int_0^R \sigma(r)dr} \ln\left(\frac{P_T(R)}{P_S(R)}\right) = \frac{1}{2\tau(R)} \ln\left(\frac{P_T(R)}{P_S(R)}\right) \tag{2}$$

where $\tau$ is the optical thickness and $P_S(R)$ is the backscatter signal due to single scattering. It should be noted that $F$ is not identical to Platt's multiple scattering factor $\eta$.[8] However, $F$ is related to $\eta$ by $F = 1 - \eta$.

ELISE's measurements will cover almost the whole globe. Due to the long time of operation (one year) a large number of different atmospheric conditions will occur which will include various types of clouds and aerosols. However, for practical reasons only a small number of representative cases can be investigated.

In the following discussion we concentrate on aerosol mixtures in the Planetary Boundary Layer (PBL). We used an atmospheric model consisting of a well-mixed PBL between 0 and 1.5km, the free troposphere above 2km with a moderate exponential decrease of aerosol extinction coefficient $\sigma$ and an intermediate layer between 1.5 and 2km with a strong decrease of aerosol extinction. The assumption of a well-mixed PBL implies a constant aerosol extinction coefficient and the relative humidity increasing with height. Hence the phase function and therefore also the lidar ratio is height-dependent. Fig. 2 shows an example of the extinction profile at 527nm for 5km visibility. The wavelength dependence of $\sigma$ was assumed to be $\lambda^{-1}$. We used similar extinction profiles for other visibilities. Aerosol data were taken from the OPAC dataset.[4] System parameters for ELISE were used as given in Tab. 1.

Fig. 3 shows that different characteristics of the aerosol types also lead to different multiple scattering intensities. In this case the extinction profile for 5km visibility was used, as shown in Fig. 2. Basically two groups can be distinguished. Group A consists of the continental types (without desert), group B includes the maritime types and the desert mixture. For group A types the ratio of multiple to single scattering intensities is about 0.3 and approximately constant in the PBL while for group B types the ratio is increasing throughout the PBL and reaches values of 0.5 to 0.6 near the ground (the far end when observed from space). The constant ratio for group A is due to the influence the relative humidity has on the phase function. The differences of the ratio for different aerosol type result mainly from their respective size distributions. For the continental types small particles are dominant. Hence, sideward scattering is more pronounced which results in a relatively smaller multiple scattering intensity to be detected. On the other side group B aerosol type contain a relatively greater portion of large particles, resulting in a more pronounced forward scattering peak. For all types multiple scattering is almost exclusively due to the second scattering order. Calculations for the longer wavelength (1053nm) show similar features, however, the ratio of multiple to single scattering intensities is only about one third of that for 527nm (without figure).

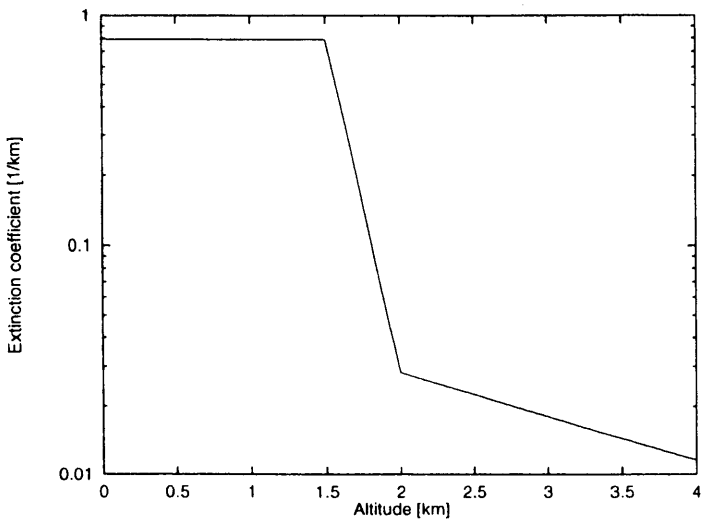


**Figure 2.** Example of an assumed extinction profile for ELISE's shorter wavelength (527nm). Here visibility is 5km.

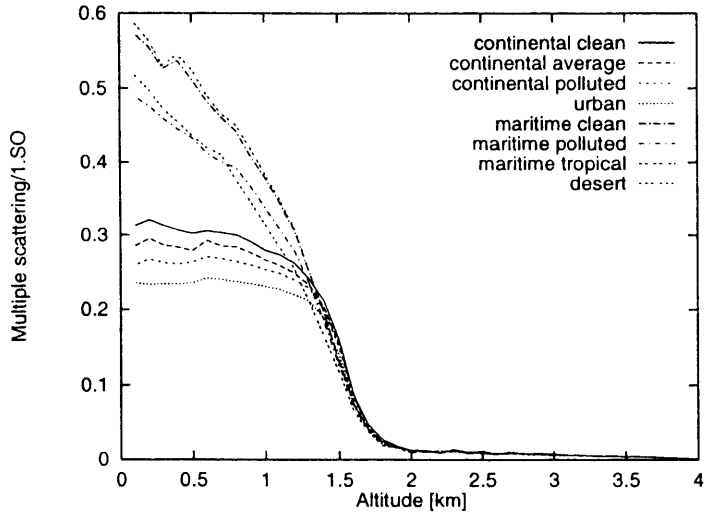


**Figure 3.** Ratio of multiple to single scattering for different aerosol types for an atmosphere with the extinction profile from Fig. 2.

Fig. 4 presents the resulting multiple scattering factor $F$ calculated with Eq. 2. Apparently, the same discrimination of the two groups of aerosol types can be found as for the multiple scattering intensitities (Fig. 3). Group A aerosols show a stronger decrease of $F$ with penetration depth into the PBL than goup B types leading to smaller values at lower altitudes. However, maximum values at the top of the PBL are larger. Fig. 5 shows that similar characteristics are also found for other visibilities between 2 and 25km (the extinction coefficient in the PBL was changed accordingly while the free troposphere remained the same). But Fig. 5 also reveals that $F$ additionally depends on the visibility, i.e. the extinction coefficient. The influence of the latter appears to be the dominant one.

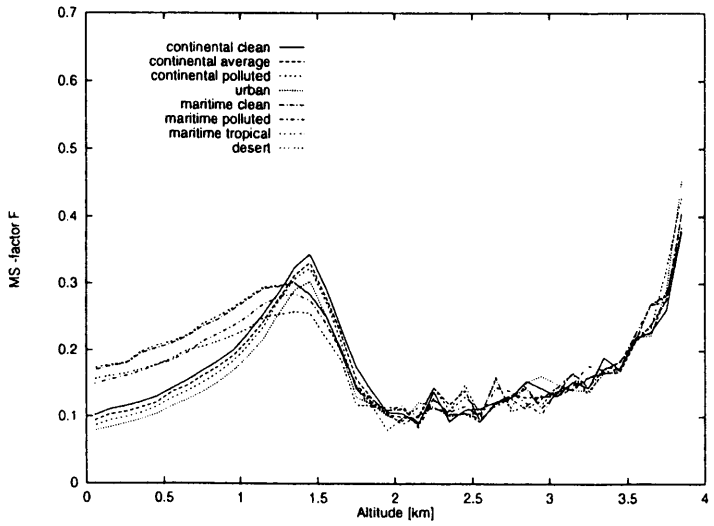


**Figure 4.** Multiple scattering factor $F$ for different aerosol types for an atmosphere with the extinction profile from Fig. 2.

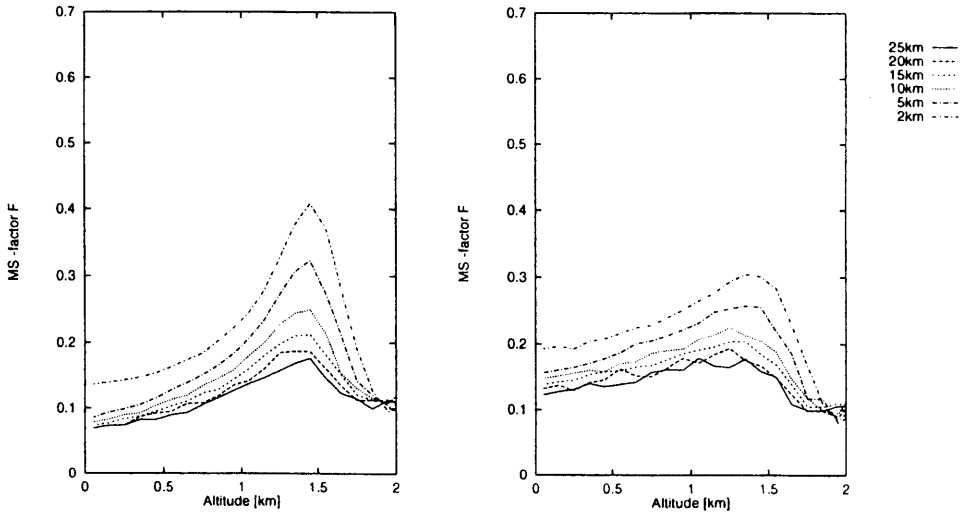


**Figure 5.** Multiple scattering factor $F$ for different visibilities. The wavelength was 527nm. (a) continental polluted; (b) desert.

## 4. OUTLOOK

Calculations showed that the multiple scattering factor $F$ in aerosol layers strongly depends on atmospheric conditions. It is a function of both extinction coefficient and aerosol mixture. In most of ELISE's measurement situations an exact estimates of $F$ won't be possible since the atmospheric conditions are not known in detail. Instead, only rough assumptions will be available. It still has to be investigated how an inexact multiple scattering factor influences the inversion of ELISE's lidar signals. This must also include the combined effect of a roughly assumptions of both $F$ and other parameters which enter the inversion (e.g. the lidar ratio).

## ACKNOWLEDGMENTS

This study has been and still is supported by the Association for International Research Initiatives for Environmental Studies (AIRIES).

## REFERENCES

1. D. M. Winker, R. H. Couch, and M. P. McCormick, "An overview of LITE: NASA's lidar in-space technology experiment," *Proc. IEEE* **84**, pp. 164–179, 1996.
2. J. Spinhirne, "Lidar clear atmosphere multiple scattering dependence on receiver range," *Appl. Opt.* **21**, pp. 2467–2468, 1982.
3. Y. Sasano, "ELISE (experimental lidar in space equipment) development and science application plan: NASDA mission demonstration satellite lidar (mds-lidar) project," in *Proceedings of the 19th ILRC, Hampton,USA*, pp. 949–953, 1998.
4. M. Heß, P. Koepke, and I. Schult, "Optical properties of aerosols and clouds: the software package OPAC," *Bull. Am. Met. Soc.* **79**, pp. 831–844, 1998.
5. A. Starkov, M. Noormohammadian, and U. Oppel, "A stochastic model and a variance-reduction monte-carlo method for the calculation of light transport," *Appl. Phys. B* **60**, pp. 335–340, 1995.
6. M. Kerscher, W. Krichbaumer, U. G. Oppel, and M. Noormohammadian, "Polarized multiply scattered lidar returns," *Opt. Rev.* **2**, pp. 304–307, 1995.
7. K. Kunkel and J. Weinman, "Monte carlo analysis of multiply scattered lidar returns," *J. Atmos. Sci.* **33**, pp. 1772–1780, 1976.
8. C. M. R. Platt, "Remote sounding of high clouds. III: Monte carlo calculations of multiple-scattered lidar returns," *J. Atmos. Sci.* **38**, pp. 156–167, 1981.